Development and Validation of a Nonlinear Fabric Model for Subsonic Parachute Aerodynamics

Anton, S.V.; Rapisarda, C.; Ross, O.J.; Mooij, E.

DOI
10.2514/1.A35583

Publication date
2023

Document Version
Final published version

Published in
Journal of Spacecraft and Rockets: devoted to astronautical science and technology

JOURNAL OF SPACECRAFT AND ROCKETS
Vol. 60, No. 6, November–December 2023

Development and Validation of a Nonlinear Fabric Model for Subsonic Parachute Aerodynamics

Sabin V. Anton,* Claudio Rapisarda,† Oliver J. Ross,‡ and Erwin Mooij§
Delft University of Technology, 2629 HS Delft, The Netherlands

https://doi.org/10.2514/1.A35583

Parachute/flow interaction is dominant in evaluating a decelerator's performance. Such interaction is characterized by nonlinear deformations and complex flow phenomena. While testing methods are available to investigate parachute performance, these are often costly and nonrepresentative of the desired flight conditions. To address the need for an accessible technique capable of modeling parachutes at the early design stages, this paper proposes a robust fluid/structure interaction methodology for three-dimensional subsonic simulations. This is attained by replacing the linear springs in Provot's equation with polynomial expressions whose coefficients are fitted to tensile test data. The nonlinear cloth algorithm is coupled with the rhoPorousSimpleFoam solver in the open-source OpenFOAM toolbox, thereby establishing an iterative process that reaches steady-state convergence in at most six iterations. The transient response is obtained from the average distributed load of the steady-state pressure field and an inertial damping contribution. The simulations are performed for two disk-gap-band parachutes and a ringsail parachute over a velocity range of ring sail 5–30 m/s. The results are compared to the experimental data measured in the Open Jet Facility of Delft University of Technology, yielding errors below 5% for the steady-state cases and overestimations in peak loads of 4.4–12.4% for the transient simulations.

Nomenclature

a	=	linear Ergun constant, Ns/m^4 (N, Newton; s, second; m, meters)
a_j	=	elastic behavior coefficient, Ns/m
b	=	quadratic Ergun constant, Ns^2/m^5
C	=	linear relative damping constant, Ns/m
C_a	=	linear absolute damping constant, Ns/m
$\boldsymbol{D}$	=	Darcy matrix, Ns/m^4
D	=	cloth characteristic length, m
D_{AP}	=	apparent parachute diameter, m
D_{ij}	=	Darcy coefficient, Ns/m^4
D_P	=	parachute diameter, m
e	=	mean shape error, m
$\boldsymbol{F}$	=	Forchheimer matrix, Ns^2/m^5
F	=	force, N
F_e	=	elastic force, N
F_{ij}	=	Forchheimer coefficient, Ns^2/m^5
K_{ax_j}	=	axial spring constant, N/m^2
K_{b_j}	=	bending spring constant, N/m^2
K_j	=	spring constant, N/m^2
K_{Max}	=	maximum spring constant, N/m^2
K_{sh_j}	=	shear spring constant, N/m^2
L	=	camera to parachute center distance, m
L_{AP}	=	apparent parachute length, m
L_0	=	undeformed spring length, m
n_s	=	unit vector perpendicular to shell
p	=	static pressure, Pa
R	=	OpenFOAM residual error
S	=	wetted surface area, m^2
S_i	=	cloth cross-section, m^2
S_0	=	parachute nominal area, m^2
t	=	thickness, m
u_j	=	scalar velocity, m/s
V	=	canopy volume, m^3
v_{rel}	=	relative velocity, m/s
X_k	=	position vector of parachute cloth points at iteration k, m
γ	=	fabric porosity
Δt	=	time step, s
Δx_e	=	elastic displacement, m
ϵ	=	bending contribution constant
$\mathcal{E}$	=	minimum R^2 value
η	=	shear contribution constant
μ	=	dynamic viscosity, kg/ms
ξ	=	mesh point mass, kg
ρ	=	air density, kg/m^3
τ_{ij}	=	viscous stress tensor, Pa
ω	=	average mesh point distance, cm

Received 10 October 2022; revision received 25 May 2023; accepted for publication 29 May 2023; published online 26 July 2023.

*Department of Space Engineering, Faculty of Aerospace Engineering; s.v.anton@student.tudelft.nl.

†Department of Space Engineering, Faculty of Aerospace Engineering; c.rapisarda@student.tudelft.nl. Member AIAA.

‡Department of Space Engineering, Faculty of Aerospace Engineering; o.j.ross@student.tudelft.nl.

§Associate Professor, Section of Astrodynamics and Space Missions, Faculty of Aerospace Engineering; e.mooij@tudelft.nl. Associate Fellow AIAA (Corresponding Author).

I. Introduction

INTEREST in parachute decelerators has been increasing since the 1960s within the context of subsonic applications in reentry, descent, and landing of space payloads, as a consequence of the provided stability and desired descent rate. Evaluating the performance of such systems, however, may be rather challenging, as the inflation of a parachute encompasses complex phenomena, such as porosity, bluff-body aerodynamics, time dependency of the flow on the deceleration of the payload, and highly deformable structures, whose shape rapidly varies as a function of the surrounding flow. As soon as the parachute is pulled out of the deployment bag, in fact, the air flows into the canopy through the parachute skirt. Although some of it leaves via the vent and other eventual openings, most air is captured within the canopy, which applies a radial pressure difference leading to a rapid inflation until the axial and radial dynamic forces and inertia of the parachute itself are balanced by the suspension-lines tension [1].

Typically, various testing methods may be performed to measure the characteristic parameters of the parachute in its transient and steady-state behavior under conditions that are as representative of the expected actual flight as physically possible. Examples of such test methods include ground-based parachute towing, wind-tunnel experiments, drop tests, and low-altitude rocket flights [2].

Nevertheless, each testing method poses disadvantages, both in terms of resources required and constraints on the parachute configuration itself and the environmental conditions to which it is subjected. In fact, not only are such tests costly, but they may also fail to account for the desired flow state. Moreover, given the iterative nature of a parachute design cycle, it would be beneficial to investigate the performance variations associated with design modifications.

It is clear that both ground testing and in-flight testing do not offer a feasible and sustainable solution at the design stage. Although such tests are required to validate the performance of the final product, the need for a flexible numerical tool capable of accurately predicting the behavior of parachutes is evident. The main motivation for this research is to increase the simulation capabilities of small companies, educational institutions, and research communities in the context of subsonic parachute deployment and flight performance, such that novel parachute designs can be investigated through the development of a high-fidelity and efficient numerical method.

Relevant studies with similar goals have been retrieved from the literature, in which computational fluid dynamics (CFD) is coupled with computational structural dynamics codes for simulating the fluid/structure interaction (FSI) phenomena. While "strong" fluid/structure interaction coupling is most suited for highly nonlinear FSI problems, such as the modeling of aerodynamic decelerator systems, the method requires solving both the fluid dynamics equations and the structural dynamics equations simultaneously, unveiling its computational impracticality. A more computationally viable approach, which is widely adopted in the literature [3], is that of separating the fluid and structural fields to interface only the interacting forces, velocities, and displacements, through what is referred to as "weak" fluid/structure coupling [4]. Among the initial weakly coupled FSI developments, LS-DYNA (Ansys LS-DYNA) was used by Vorticity, Ltd., to simulate the parachute inflation of Huygens [5] and Mars Science Laboratory [6]. The simulations were capable of capturing phenomena, such as partial collapse and reinflation of the parachute canopy. The wide application of LS-DYNA for FSI modeling was supported by its MAT_FABRIC material function, capable of modeling nonlinear stress/strain relationships [7–9]. However, this could not account for the bending and compressive stiffness of the parachute [10,11]. The Favre-filtered Navier–Stokes equations have been used by Yu et al. [12] with a Cartesian adaptive mesh to investigate the effect of large period sustained oscillations in parachutes, revealing the strong dependency between the presence of oscillations and grid resolution. This led to the conclusion that to capture transient behavior in the numerical simulator a fine mesh and, therefore, high computational capabilities are required. Because of these limitations, th implementation of immersed or embedded boundary methods has become dominant in the more recent literature to characterize large topological deformations and rotations [13]. The inflation of a parachute has been studied by the joint research initiative between the Farhat Research Group at Stanford University and NASA Jet Propulsion Laboratory [14], which proposes an unstructured, embedded boundary method based upon the compressible Navier–Stokes equations with an adaptive mesh refinement [15]. Interestingly, this work takes into consideration the initial folding state of the parachute, which can be modeled as being porous, orthotropic, and materially nonlinear,
to predict the stress distribution on the canopy, as well as the drag history and performance throughout its operations. Kim and Peskin [16,17] implemented the immersed boundary method to model semi-open parachutes in both two and three dimensions for small Reynolds numbers, while Purvis [18,19] used springs in a cylindrical coordinates frame to model the forebody structure, the suspension lines, and the canopy of the parachute. The development of alternative structural dynamics models for parachutes was prompted by the challenges pertaining to traditional finite-element method (FEA) approaches. Examples include their inability to handle large displacements using standard linear stress/strain theory, model fabric wrinkling in compression and account for the degree of anisotropy present in parachute materials [4]. Grounding on the limitations posed by FEA, Strickland et al. [20] developed the PURL algorithm in which mass is added to the structural nodes, based on the diagonally added mass matrix depending on the actual pressure and the pressure associated with this added mass. More recently, Li [21] developed a detailed analytical model of the spring system to model fabric surfaces for parachute canopies, which, however, only accounts for a linear elastic response.

The aim of the present paper is to present a novel nonlinear spring-mass model, comprising decoupled axial, shear, and bending springs, which incorporates empirical stiffness data for each of the three major parachute components, namely, fabric, seams, and suspension lines. The validity of the model is established through the consistent agreement attained between the experimental drag performance of three parachutes and the results from two numerical drag analyzes: a steady-state analysis conducted through the loose coupling between the numerical canopy and the flow, defined with the OpenFoam flow solver, where the Darcy–Forecheimer porosity model is implemented, and a transient inflation analysis, where the aerodynamics are modeled through empirically determined damping terms applied to the cloth mesh.

Following the brief literature review presented in the Introduction to contextualize the identified need for this work, the case studies investigated are outlined in Sec. II along with their key design dimensions. The methodology is described in Sec. III, focusing on the modeling of the canopy cloth material, the implementation of experimental tensile test data, and the computational modeling of the flow surrounding the parachute. Section III.E illustrates the iterative procedure developed to couple the structural deformation of the parachute cloth material with the flow dynamics for both steady-state and transient conditions. The simulation results are presented in Sec. IV and compared to experimental data. Finally, the conclusions are drawn in Sec. V.

II. Case Studies

The Parachute Research Group (PRG) within the Delft Aerospace Rocket Engineering (DARE) society, a Delft University of Technology associated student rocketry organization, has been improving available recovery systems, while also developing innovative concepts for various projects over the past few years, such as Aether, Stratos III, Stratos IV, SPEAR, SPEAR II, and SHEAR [22–27]. Among such systems, three different parachutes are hereby presented, as they constitute the case studies for this work.

A. Stratos IV Main Parachute

The first recovery system proposed in this paper is the main parachute developed for the Stratos IV mission, the fourth generation in the Stratos sounding-rocket family. The parachute is a disk-gap-band (DGB) type, which has been designed to be deployed in the subsonic regime with the goal of slowing down and retrieving the rocket nose cone [28]. The material used for the canopy entailing both the disk and the band is Nylon F111, whereas Twaron material was used for the suspension lines and the reinforcement tape. The key design dimensions of the parachute are summarized in Table 1, and a picture of the parachute is shown in Fig. 1.

Table 1 Key design parameters of the three case studies developed within PRG

Parachute	Nominal area, m^2	Disk diameter, m	Vent diameter, m	Gap height, m	Band height, m	Number of suspension lines	Length of suspension lines, m	Number of gores	Number of sails per gore
Stratos IV	1.72	1	0.09	0.07	0.3	18	1.5	6	— —
WALRUS	3.37	1.3	0.17	0.085	0.4	18	2	6	— —
ADEPT	0.79	1	0.06	— —	— —	8	1.15	8	9

Fig. 1 Stratos IV DGB main parachute.

B. WALRUS Main Parachute

The second simulated design is the one devised within the WALRUS project for the main DGB parachute in Fig. 2. Although a DGB type is already proposed as the Stratos IV main parachute, the simulation of two different designs of the same class is considered relevant for the analysis of scaling effects on the stability and overall performance of the decelerators in relation to the numerical simulation. In fact, as shown in Table 1, the WALRUS parachute is based upon the Stratos IV heritage and is a scaled-up version of the latter. Nylon F111 is used for the canopy cloth, while Spectra material was chosen for the suspension lines.

C. Ringsail Parachute

To prove the extensive modeling capabilities of the numerical simulation proposed in this paper, an alternative decelerator type to the two aforementioned DGBs is hereby considered. The ringsail parachute shown in Fig. 3 developed within the ADEPT project is therefore chosen as the third case study. For this design, Nylon F111 was also used to manufacture the canopy, and Twaron was used for the suspension lines and reinforcement tape.

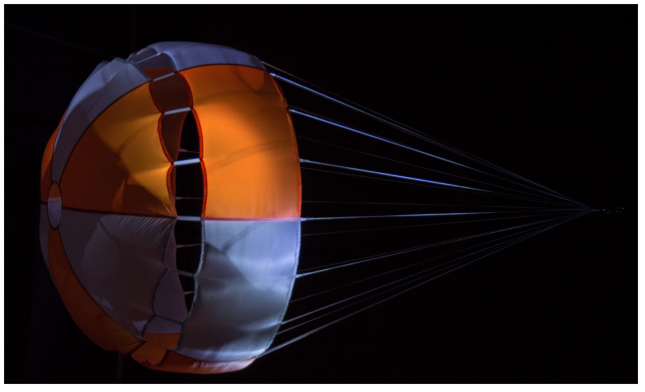

Fig. 2 WALRUS DGB main parachute.

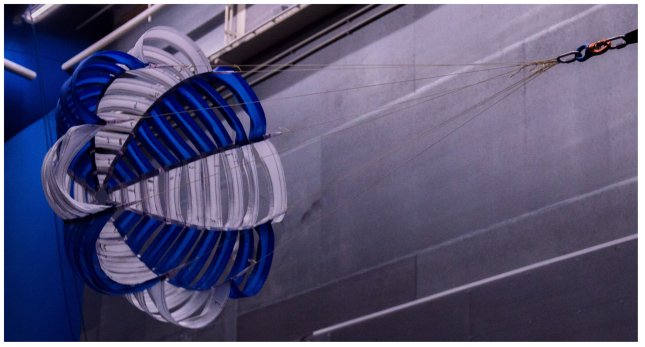

Fig. 3 ADEPT Ringsail parachute.

D. Open Jet Facility

To provide a means of validation to the applied numerical simulation, the three outlined case studies have been tested in the Open Jet Facility (OJF) wind-tunnel at the High-Speed Laboratory of Delft University of Technology. This entails a closed-loop, open test section with an octagonal exit area of 2.85×2.85 m^2 and a 3:1 contraction ratio in a 13 m wide and 8 m high room, suitable for research on parachutes of relatively large dimensions. The facility is powered by a 500 kW electric motor, which is capable of achieving a maximum freestream speed of around 35 m/s and dynamic pressures up to 0.5 kPa [29]. The experimental drag and stability data are thus used for comparison with the simulation results under reproducible conditions.

III. Methodology

A. Canopy Fabric Modeling

1. *Established Cloth Simulation Algorithms*

In general, parachute canopies are made from woven fabrics with a high tear resistance, requiring materials such as Ripstop Nylon, or Kevlar [30]. Modeling these types of fabrics numerically, in the context of FSI simulations, has historically been done using FEA. Although such an analysis is suitable for relatively stiff, elastic structures, it has proven impractical for aerodynamic decelerators. [4] This is first due to the highly nonlinear, elastic, and anisotropic nature of parachute fabric, which makes linear stress/strain theory nonapplicable. Second, FEA fails to model the wrinkling observed in parachute canopies in regions with compressive loads [4]. This illustrates the need for specialized cloth algorithms for reentry applications. In known literature, three approaches distinguish themselves for simulating cloth behavior. The first class of methods, used in early studies, involves the use of known geometrical deformations for the determination of hanged cloth static behavior [31,32]. Such methods fail to model the dynamic behavior of cloth as well as their deformation under extreme loads and, therefore, were not considered in this study. In the early 1990s, a new class of physically rooted methods arose, which uses elastically deformable mass-spring models based on Hooke's law to model the axial, shear, and bending deformations in woven fabrics. One of the most popular models of this kind was proposed by Provot et al. [33] and consists of discretizing cloth as a grid of lumped-mass points, linked by linear, elastic springs. The dynamic behavior of the cloth is then computed through simple, explicit time-integration schemes. While fairly robust and intuitive, this method fails to model anisotropic fabric deformation under high, localized loads due to a phenomenon called *superelasticity*, which leads to unnaturally high stretching at the points of the applied external forces. This phenomenon is shown in Fig. 4. This figure shows two simulated parachute meshes. The parachute above is simulated with a nonlinear mass-spring model, whereas the one below makes use of a linear one. It can be observed that the parachute below is considerably more stretched than the one above it, for the same pressure loading.

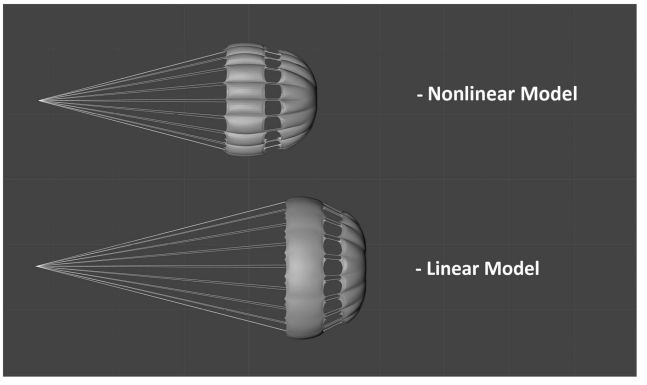

Fig. 4 The superelasticity phenomenon illustrated by two simulated parachutes under the same load.

Provot [33] solves this issue by imposing a maximum allowed stretch criterion on the cloth springs, which counters the high deformations. However, doing so leads to incorrect physical responses in the cloth, which makes the model unsuitable for engineering applications. The most recent developments in cloth simulation involve the use of energy methods to compute the elastic deformations in springs, as done by Baraff and Witkin [34]. This class of methods is known to yield the most realistic cloth behavior, but it does so at the expense of high computational effort, as it uses implicit numerical schemes. Furthermore, much like mass-spring models, it is limited to linear elastic behavior.

2. *Nonlinear Mass-Spring Model*

For the purposes of this study, the method proposed by Provot [33] has been chosen, as it poses two main advantages. First, it is an explicit method with a sparse system matrix, implying relatively low computational power and memory requirements. Second, unlike energy methods, it allows for the decoupling of normal, shear, and bending stress contributions, which are treated separately. This makes the correlation with experimental stress/strain data on isolated load cases trivial. Even with these advantages, the linear nature of the method makes its use in parachute decelerator applications limited. To solve the aforementioned superelasticity problem and obtain physically accurate stresses and strains in anisotropic canopy fabric, a novel approach is proposed, involving the modeling of nonlinear springs, based on the real properties of the fabric. Such an approach would allow accurate modeling of fabric wrinkling at high loads, based on the reasoning in [4]. The original ordinary differential equation for the cloth springs, proposed by Provot for one spring of one lumped-mass point, is given by [33],

$$\zeta \frac{d^2\boldsymbol{X}}{dt^2} = \frac{\boldsymbol{X}-\boldsymbol{X_i}}{|\boldsymbol{X}-\boldsymbol{X_i}|}\left[K(|\boldsymbol{X}-\boldsymbol{X_i}|-L_0) + C\frac{d(\boldsymbol{X}-\boldsymbol{X_i})}{dt}\frac{\boldsymbol{X}-\boldsymbol{X_i}}{|\boldsymbol{X}-\boldsymbol{X_i}|}\right] \tag{1}$$

where ζ is the mass of the point in kilograms; $\boldsymbol{X}$ is the position vector of the point in meters; $\boldsymbol{X_i}$ is the position vector of the neighboring point connected to the one in question in meters; K is the linear constant of the spring in Newtons/meter; and C is the relative, linear damping coefficient of the spring in Ns/m. This equation is modified to model nonlinear elastic behavior by replacing the linear spring responses with nth-order polynomials, approximating the force-displacement curves of the fabric fibers in a given orientation. Thus, Eq. (1) is extended as

$$\zeta \frac{d^2\boldsymbol{X}}{dt^2} = \frac{\boldsymbol{X}-\boldsymbol{X_i}}{|\boldsymbol{X}-\boldsymbol{X_i}|}\left\{\left[\sum_{j=1}^{n} K_j\left(\frac{|\boldsymbol{X}-\boldsymbol{X_i}|}{L_0}-1\right)^j S_i\right] + C\frac{d(\boldsymbol{X}-\boldsymbol{X_i})}{dt}\frac{\boldsymbol{X}-\boldsymbol{X_i}}{|\boldsymbol{X}-\boldsymbol{X_i}|}\right\} \tag{2}$$

where n is an arbitrary number representing the polynomial degree, S_i (in meters squared) is the cross-section of the cloth element in direction $(\boldsymbol{X}-\boldsymbol{X_i})/(|\boldsymbol{X}-\boldsymbol{X_i}|)$, and K_j are nonlinear spring constants (in Newtons/meters squared). The indices j signify the powers of the displacement terms in the polynomial, which, when multiplied with the proportionality constants K_j, model the nonlinear behavior of the fabric. With the correct constants, this equation solves the problem of superelasticity and captures the stiffening effect of fabric under extreme tension mentioned in [33], which is necessary for the study of parachute inflation behavior. One downside of this nonlinear system, though, is that it becomes stiffer with increasing applied loads. This is solved, however, by combining it with a high-order time-integration scheme and choosing a small-enough time step.

Figure 5 shows the spring matrix used by the cloth model, against a sketch of real woven fabric used in parachute canopies. The matrix is a two-dimensional representation of the fabric, accounting for the most important of its elastic properties. Equation (2) is applied to all the 12 springs connecting a point (i, j) to its 12 neighboring points, yielding 12 acceleration contribution vectors, which are summed up to compute $(d^2\boldsymbol{X}/dt^2)_{ij}$. The springs used by this mesh are classified as follows:

1) There are four axial springs connecting points $(i, j+1)$, $(i, j-1)$, $(i+1, j)$, and $(i-1, j)$ to point (i, j). The springs are oriented at 0 and 90 deg and represent the contribution of an arbitrary number of canopy fibers, depending on the preset resolution of the mesh.

2) There are four shear springs connecting the points $(i+1, j+1)$, $(i+1, j-1)$, $(i-1, j+1)$, and $(i-1, j-1)$ to point (i, j). The springs are oriented at 45 deg and account for the friction and compression forces between the woven fibers under a force acting at 45 deg with respect to their orientation.

3) There are four bending springs connecting the points $(i+2, j)$, $(i-2, j)$, $(i, j+2)$, and $(i, j-2)$ to point (i, j). The springs are oriented at 0 and 90 deg and model the resistance of the canopy fibers to an applied bending moment.

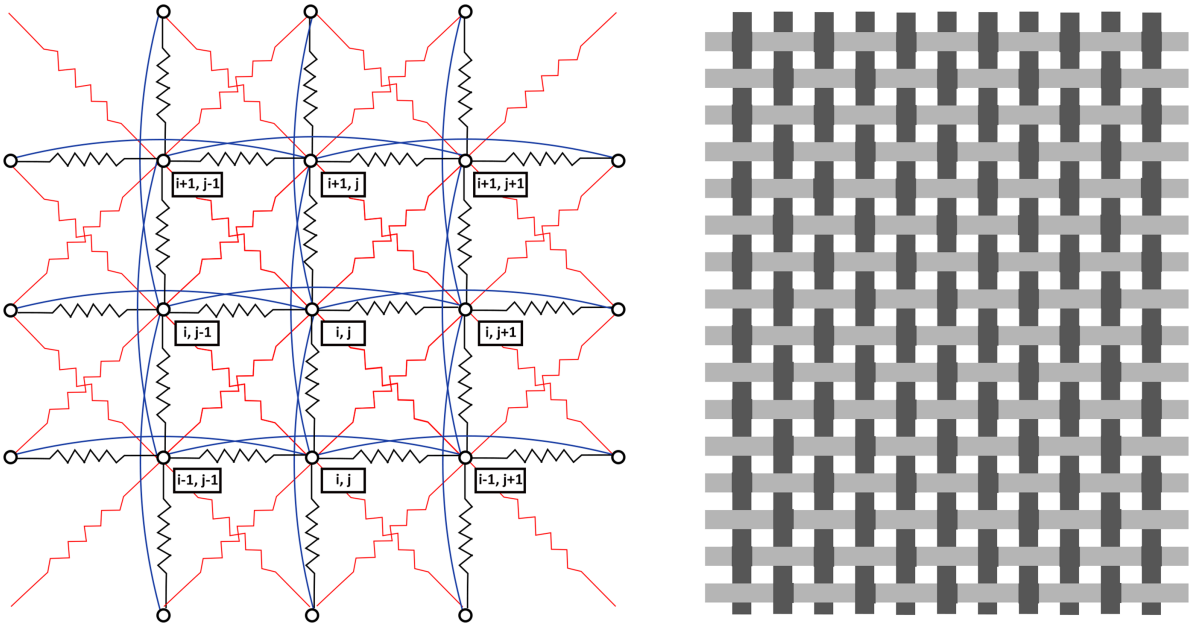

Fig. 5 Left: parachute canopy nonlinear mass-spring model. Axial springs are shown in black, shear springs are in red, and bending springs are in blue. Right: a sketch of a typical canopy two-directional fabric fiber pattern. The light and dark gray fibers may have different elastic properties.

These springs model three types of resistance forces in the fibers of the fabric. Intuitively, the axial springs account for the elastic resistance of the fibers against stretching. The shear springs, however, partly account for the resistance of the fibers from Fig. 5 (right) to lateral compression, when loaded in a 45 deg orientation. These compressive forces are correlated to the distance between two parallel fibers, as well as their diameter. Consequently, the bending springs account for the fiber resistance to axial compression due to bending. For this mesh, the proposed nonlinear cloth model in Eq. (2) is discretized as

$$\begin{aligned}\zeta\ddot{\boldsymbol{X}}_{ij} = &\sum_{a,b}\frac{\boldsymbol{X}_{i+a,j+b}-\boldsymbol{X}_{ij}}{|\boldsymbol{X}_{i+a,j+b}-\boldsymbol{X}_{ij}|}\\ &\times\left[\sum_{k=1}^{n}K_{k_{i+a,j+b}}\left(\frac{|\boldsymbol{X}_{i+a,j+b}-\boldsymbol{X}_{i,j}|}{L_{0_{i+a,j+b}}}-1\right)^{k}S_{ijab}\right]\\ &+C\sum_{a,b}(\dot{\boldsymbol{X}}_{i+a,j+b}-\dot{\boldsymbol{X}}_{ij})\frac{\boldsymbol{X}_{i+a,j+b}-\boldsymbol{X}_{ij}}{|\boldsymbol{X}_{i+a,j+b}-\boldsymbol{X}_{ij}|}\frac{\boldsymbol{X}_{i+a,j+b}-\boldsymbol{X}_{ij}}{|\boldsymbol{X}_{i+a,j+b}-\boldsymbol{X}_{ij}|}\end{aligned} \tag{3}$$

with $(a,b)\in\{(u,v)|u\in\{-1,0,1\},v\in\{-1,0,1\}\}\setminus(0,0)$.

A one-dimensional spring mesh, similar to the one shown in Fig. 5, has been used to model the suspension lines of parachutes. For this mesh, only two axial springs were used, $(i+1,j)$ and $(i-1,j)$, together with two bending springs, $(i+2,j)$ and $(i-2,j)$. Hence, the equation of motion for the mesh points simplifies to

$$\begin{aligned}\zeta\ddot{\boldsymbol{X}}_{i} = &\frac{\boldsymbol{X}_{i\pm1}-\boldsymbol{X}_{i}}{|\boldsymbol{X}_{i\pm1}-\boldsymbol{X}_{i}|}\left[\sum_{k=1}^{n}\hat{K}_{k_{\text{norm}}}\left(\frac{|\boldsymbol{X}_{i\pm1}-\boldsymbol{X}_{i}|}{L_{0_{i\pm1}}}-1\right)^{k}L_{i_{\text{norm}}}\right.\\ &\left.+\sum_{k=1}^{n}\hat{K}_{k_{\text{bend}}}\left(\frac{|\boldsymbol{X}_{i\pm2}-\boldsymbol{X}_{i}|}{L_{0_{i\pm2}}}-1\right)^{k}L_{i_{\text{bend}}}\right]\\ &+C(\dot{\boldsymbol{X}}_{i\pm1,2}-\dot{\boldsymbol{X}}_{i})\frac{\boldsymbol{X}_{i\pm1,2}-\boldsymbol{X}_{i}}{|\boldsymbol{X}_{i\pm1,2}-\boldsymbol{X}_{i}|}\frac{\boldsymbol{X}_{i\pm1}-\boldsymbol{X}_{i}}{|\boldsymbol{X}_{i\pm1,2}-\boldsymbol{X}_{i}|}\end{aligned} \tag{4}$$

This equation comes with the added subtlety that the $\hat{K}$ coefficients have units of Newtons/meter instead of Newstons/meter squared. Figure 6 shows this discretization. The final modeling aspects to be treated are that of parachute seams, where reinforcement tape is added, and the connection between the suspension lines and the canopy, at the parachute seams. A sketch of the former is provided in Fig. 7. For the canopy areas covered in reinforcement tape, a

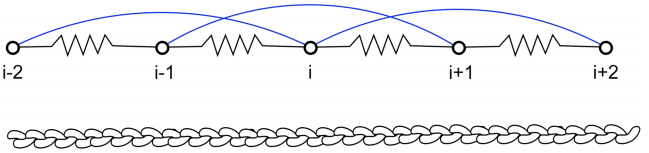

Fig. 6 Above: a sketch of typical woven fabric used for parachute suspension lines. Below: the nonlinear mass-spring discretization for the suspension lines. Axial springs are shown in black, and bending springs are in blue.

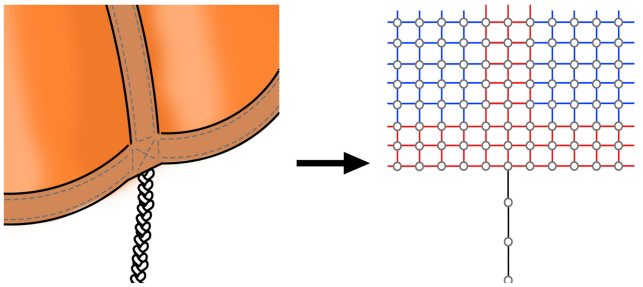

Fig. 7 Left: a sketch of the connection point between the parachute and one suspension line. Right: the mass-spring treatment of this connection point.

superposition of forces assuming springs in parallel is performed, which only affects the numerical values of the polynomial spring constants in Eq. (11). The connection point, however, requires a particular equation of motion:

$$\begin{aligned}\zeta\ddot{\boldsymbol{X}}_{i} = &\sum_{a,b}\frac{\boldsymbol{X}_{i+a,j+b}-\boldsymbol{X}_{ij}}{|\boldsymbol{X}_{i+a,j+b}-\boldsymbol{X}_{ij}|}\\ &\times\left[\sum_{k=1}^{n}K_{k_{i+a,j+b}}\left(\frac{|\boldsymbol{X}_{i+a,j+b}-\boldsymbol{X}_{i,j}|}{L_{0_{i+a,j+b}}}-1\right)^{k}S_{ijab}\right]\\ &+C(\dot{\boldsymbol{X}}_{i\pm1,2}-\dot{\boldsymbol{X}}_{i})\frac{\boldsymbol{X}_{i\pm1,2}-\boldsymbol{X}_{i}}{|\boldsymbol{X}_{i\pm1,2}-\boldsymbol{X}_{i}|}\frac{\boldsymbol{X}_{i\pm1}-\boldsymbol{X}_{i}}{|\boldsymbol{X}_{i\pm1,2}-\boldsymbol{X}_{i}|}\\ &+\frac{\boldsymbol{X}_{i-1}-\boldsymbol{X}_{i}}{|\boldsymbol{X}_{i-1}-\boldsymbol{X}_{i}|}\left[\sum_{k=1}^{n}\hat{K}_{k_{\text{norm}}}\left(\frac{|\boldsymbol{X}_{i-1}-\boldsymbol{X}_{i}|}{L_{0_{i-1}}}-1\right)^{k}L_{i_{\text{norm}}}\right.\\ &\left.+\sum_{k=1}^{n}\hat{K}_{k_{\text{bend}}}\left(\frac{|\boldsymbol{X}_{i-2}-\boldsymbol{X}_{i}|}{L_{0_{i-2}}}-1\right)^{k}L_{i_{\text{bend}}}\right]\\ &+C(\dot{\boldsymbol{X}}_{i-1,2}-\dot{\boldsymbol{X}}_{i})\frac{\boldsymbol{X}_{i-1,2}-\boldsymbol{X}_{i}}{|\boldsymbol{X}_{i-1,2}-\boldsymbol{X}_{i}|}\frac{\boldsymbol{X}_{i-1}-\boldsymbol{X}_{i}}{|\boldsymbol{X}_{i-1,2}-\boldsymbol{X}_{i}|}\end{aligned} \tag{5}$$

with $(a,b)\in\{(u,v)|u\in\{0,1\},v\in\{0,1\}\}\setminus(0,0)$.

Equation (5) reveals a significant shortcoming of the one-dimensional discretization for the suspension lines: the emergence of large stress concentrations due to neglecting the suspension line thickness. This is solved through the use of nonlinear springs, that scale with their initial length with the power of their polynomial order. However, such a procedure will come at the cost of an augmented time constraint.

B. Time Integration and Stability Analysis

The numerical time integration of the proposed cloth model is performed using a semi-implicit Euler method. This method has been chosen due to its balance between accuracy and computational complexity [35]. Denoting the second derivative of the lumped mass point position at time $n\Delta t$, $\ddot{\boldsymbol{X}}^{n}=\boldsymbol{F}(\boldsymbol{X}^{n},\boldsymbol{V}^{n})$, $\boldsymbol{V}^{n}=\dot{\boldsymbol{X}}^{n}$, the scheme is as follows:

$$\begin{pmatrix}1 & 0\\ -\Delta t & 1\end{pmatrix}\begin{pmatrix}\boldsymbol{V}^{n+1}\\ \boldsymbol{X}^{n+1}\end{pmatrix}=\begin{pmatrix}\boldsymbol{V}^{n}\\ \boldsymbol{X}^{n}\end{pmatrix}+\Delta t\begin{pmatrix}\boldsymbol{F}(\boldsymbol{X}^{n},\boldsymbol{V}^{n})\\ 0\end{pmatrix} \tag{6}$$

To analyze the stability of this time-integration method applied to the model, the damping terms in Eq. (3) are neglected, for a conservative estimation of the time step constraint. At the same time, the external forces applied on each spring are neglected to obtain a homogeneous differential equation, and the springs are assumed to be linear, with a $K_{\max}=\max(dF_e/d\epsilon_{\text{st}})$:

$$\begin{aligned}\begin{pmatrix}1 & 0\\ -\Delta t & 1\end{pmatrix}\begin{pmatrix}\boldsymbol{V}^{n+1}\\ \boldsymbol{X}^{n+1}\end{pmatrix}=\begin{pmatrix}1 & -\omega^{2}\Delta t\\ 0 & 1\end{pmatrix}\begin{pmatrix}\boldsymbol{V}^{n}\\ \boldsymbol{X}^{n}\end{pmatrix}\Leftrightarrow\begin{pmatrix}\boldsymbol{V}^{n+1}\\ \boldsymbol{X}^{n+1}\end{pmatrix}\\ =\begin{pmatrix}1 & 1-\omega^{2}\Delta t\\ \Delta t & 1-\omega^{2}\Delta t^{2}\end{pmatrix}\begin{pmatrix}\boldsymbol{V}^{n}\\ \boldsymbol{X}^{n}\end{pmatrix}\end{aligned} \tag{7}$$

In this linearized formulation, where $\omega=\sqrt{(k_{\max}/m)}$, m being the mass of one point in the mesh and $k_{\max}$ being the dimensional bound on the spring constants of the mesh, a von Neumann stability analysis is performed for the numerical scheme, assuming $\boldsymbol{X}^{n}=\hat{X}e^{I\omega t}$ and $\boldsymbol{V}^{n}=I\omega\hat{V}e^{I\omega t}$. Requiring $|(\boldsymbol{X}^{n+1}/\boldsymbol{X}^{n})|\leq 1$ for stability, and substituting these forms in the second row of the system in Eq. (7) yields the constraint on the numerical time step,

$$\Delta t\leq\Delta x\sqrt{\frac{\rho_s\Delta x}{K_{\max}S_{ij_{\max}}}} \tag{8}$$

with ρ_s being the surface density of the material fabric (kilograms/meters squared), $S_{ij_{\max}}$ being the maximum surface of the panels in the computational mesh, and Δx being the initial length of the smallest spring in the numerical mesh. A similar condition can be written for the stability of the suspension line meshes,

$$\Delta t \leq \Delta x \sqrt{\frac{\rho_l}{\hat{K}_{\max} L_{i_{\max}}}} \tag{9}$$

where ρ_l is the line density of the suspension line (kilogram/meter) and $L_{i_{\max}}$ is the maximum length of the segments in the computational line mesh. A final note about this analysis pertains to the computation of $K_{\max}$ and $\hat{K}_{\max}$. Obtaining these constants for a material requires knowledge of the entire stress/strain curve up to the failure stress. This emphasizes the need for experimental tensile test data for all the materials in a parachute to obtain accurate behavior for the numerical mesh and choose suitable numerical simulation parameters.

C. Cloth Model Refinement with Experimental Data

1. Experimental Setup

As mentioned by Provot [33], one of the difficulties in simulating cloth fabric with a lumped mass-spring model is correlating the spring constants to real, cloth-material properties. The improved model proposed in this study imposes even larger challenges, as the nonlinear elastic response modeled with nth degree polynomials in Eq. (2) implies that multiple constants must be solved per spring. For example, if one chooses to describe the elastic response with second-degree polynomials, three spring constants must be solved per spring type, resulting in six constants for every mass node, compared to the three required for a linear model. To accomplish this feat, an empirical approach was chosen: several tensile tests have been conducted on F-111 Nylon woven fabric samples, at three fiber orientations: 0, 45, and 90 deg. Furthermore, tests have been performed on Spectra rope samples, which were used as parachute suspension lines, as well as F-111 Nylon reinforcement tape, which was used to connect parachute gores together. For each test, a force-displacement curve has been recorded up to the failure of the sample. The experimental setup for the tests is shown in Fig. 8.

It consists of a rectangular sample friction, clamped at both ends using two rubber sheets at each end, held together by a hydraulic system. The bottom clamp is then pulled to enforce a strain on the fabric, and its reaction force is recorded using a load cell installed on the top clamp. The pressure applied on the rubber sheets was set to 60 bar, while the pulling velocity of the bottom clamp was set to the maximum allowed of 50 cm/min, to simulate the shocks experienced by parachute in flight. A summary of the tests performed for this study is given in Table 2.

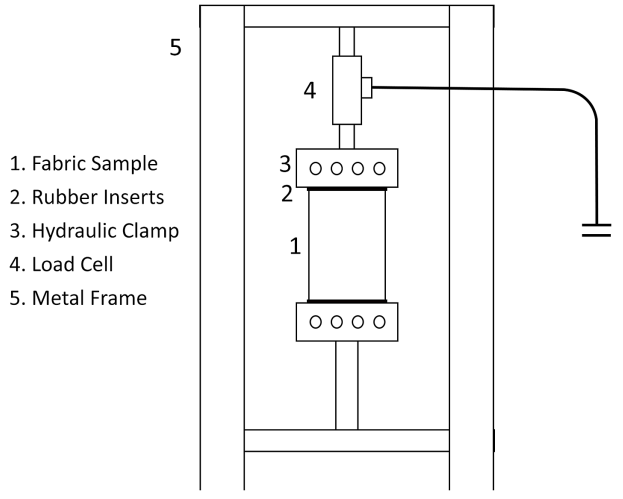

Fig. 8 Sketch of the experimental setup for the tensile test of parachute fabric.

Table 2 Summary of the mechanical tensile tests performed on samples of parachute cloth materials

Type of test	Material	Number of samples	Orientation, deg
Canopy sample test	F-111 Ripstop Nylon	3	0
Canopy sample test	F-111 Ripstop Nylon	3	90
Canopy sample test	F-111 Ripstop Nylon	3	45
Reinforcement tape test	F-111 Ripstop Nylon	3	— —
Suspension line test	Spectra	3	— —

Every test yielded two sets of data points, which describe two functions of time: the displacement $\Delta x_e = \Delta x_e(t)$ (millimeters) and the tensile resistance $F_e = F_e(t)$ (Newtons).

The mean stress/strain curve for each test condition was used to compute a specific set of spring constants in the cloth model. The procedure to do so is different for the two-dimensional canopy material vs the one-dimensional suspension lines. The former shall be explained first, as it is more involved.

2. Canopy Material Modeling and Refinement

The spring elastic behavior of the canopy woven fabric is determined as follows. A user-chosen polynomial degree n is used to model the 0 and 90 deg axial spring behaviors, such that the force-displacement curves observed in the tensile tests for these orientations are recreated by the numerical mesh with sufficient accuracy. The model is considered accurate if the coefficient of determination $R^2 > \mathcal{E}$, for the force-displacement curves in both orientations, where $\mathcal{E}$ is an arbitrarily chosen minimum R^2 value. For this study, a minimum R^2 value of $\mathcal{E} = 0.95$ was chosen, which yielded a necessary polynomial degree of 2. These fiber orientations are chosen because the tensile load is primarily carried by the fibers parallel to the load path, while other contributions are negligible. Next, a least-squares regression method is used on the Δx_e and F_e data sets to determine the n constants describing this polynomial, for m data points in a recorded set $m > n$:

$$\begin{pmatrix} 1 & \frac{\Delta x_{e0}}{L_0} & \cdots & \left(\frac{\Delta x_{e0}}{L_0}\right)^n \\ 1 & \frac{\Delta x_{e1}}{L_0} & \cdots & \left(\frac{\Delta x_{e1}}{L_0}\right)^n \\ \vdots & & & \vdots \\ 1 & \frac{\Delta x_{em}}{L_0} & \cdots & \left(\frac{\Delta x_{em}}{L_0}\right)^n \end{pmatrix} \begin{pmatrix} a_0 \\ a_1 \\ \vdots \\ a_n \end{pmatrix} = \frac{1}{W_0} \begin{pmatrix} F_{e0} \\ F_{e1} \\ \vdots \\ F_{em} \end{pmatrix} \tag{10}$$

The displacements are transformed into engineering strain using the initial length of the sample L_0, while the elastic forces are transformed into distributed loads by dividing them with the width of the sample W_0. The equation yields n coefficients $a_0, a_1, \ldots, a_n$, in Newtons/meter, which need to be multiplied with the width of a mass element in the computational cloth mesh to yield the polynomial constants $K_0, K_1, \ldots, K_n$ for 0 and 90 deg axial springs. The shear and bending spring polynomial constants are found through a different procedure altogether. As their purpose in the model is to account for the interfiber frictional forces and bending resistance, they are considered to be a function of the fiber diameter and E modulus. Therefore, in the computational model, the shear and bending spring coefficients are assumed to be linearly related to the axial coefficients by the constants ξ, $0 \leq \xi < 1$, and ϵ, with $0 \leq \epsilon < 1$. The corrected axial, shear, and bending spring polynomial coefficients for the cloth are therefore given by

$$\begin{pmatrix} K_{ax_0} \\ K_{ax_1} \\ \vdots \\ K_{ax_n} \end{pmatrix} = (1-\xi-\epsilon)\begin{pmatrix} K_0 \\ K_1 \\ \vdots \\ K_n \end{pmatrix}, \quad \begin{pmatrix} K_{sh_0} \\ K_{sh_1} \\ \vdots \\ K_{sh_n} \end{pmatrix} = \frac{\xi}{2}\begin{pmatrix} K_0 \\ K_1 \\ \vdots \\ K_n \end{pmatrix}, \quad \begin{pmatrix} K_{b_0} \\ K_{b_1} \\ \vdots \\ K_{b_n} \end{pmatrix}$$

$$= \frac{\epsilon}{2}\begin{pmatrix} K_0 \\ K_1 \\ \vdots \\ K_n \end{pmatrix} \tag{11}$$

The constants ξ and ϵ are determined by minimizing the error between the experimental shear stress curve and a simulated curve for angles of 45 and 0/90 deg. For this study, it was found that $\xi = 0.2$ and $\epsilon = 0.01$ yield the most accurate cloth behavior in all orientations considered, with $R^2 > 0.95$. The optimization process involved numerically reconstructing the tested canopy samples using the nonlinear model, applying the same test loads at their bottom end, and recording the stress distributions and reaction forces. This was done for several values of ξ and ϵ, until the error between the experimental and simulated force-displacement curves was minimized for all orientations considered.

3. *Suspension Line Refinement*

The procedure of determining the nonlinear spring constants for modeling parachute suspension lines using the proposed cloth system and experimental force-displacement data is very similar to the one used for the canopy material. The main difference between the two approaches is the absence of shear springs in the suspension line spring mesh, which removes the need for the constant ξ in Eq. (11). Furthermore, as suspension lines do not have a considerable width, the parameter W_0 is removed from Eq. (10), which results in the polynomial constants $a_0, a_1, \ldots, a_n$ having the same units as $K_0, K_1, K_2, \ldots, K_n$, namely, Newtons.

D. Steady-State Computational Modeling of Flow Surrounding Parachute

To determine the steady-state aerodynamic behavior of the parachutes considered in Sec. II, the Reynolds-averaged Navier–Stokes equations were solved on a volume containing the numerical parachute mesh, for a fluid with a constant incoming inlet velocity matching the real wind-tunnel speed. The parachute canopy is modeled for this simulation as a porous medium, using a Darcy–Forchheimer source term. For this analysis, the OpenFOAM open-source library has been used [36]. The drag sources from the parachute suspension lines are neglected for simplicity and robust meshing, as it is considered negligible in comparison to the canopy drag (less than 2% for Stratos IV), based on a simple computation assuming a cylindrical cross-section of a 2.5 mm radius, and the drag coefficients found in the work by Bergeron et al. [37] for Spectra lines, in comparable flow conditions.

1. *OpenFOAM Case Setup*

The OpenFOAM simulations are meshed with a Cartesian grid. The three-dimensional computational domain is represented by a box with the width and height matching the dimensions of the test region in the Open Jet Facility (OJF) wind tunnel [39], where the flow is smooth, near laminar. A schematic of this wind tunnel is shown in Fig. 9. The length of the domain was chosen as the distance between the wind-tunnel inlet and the point where the safety mesh is attached. These dimensions were chosen to replicate the minor wake effects that may be observed in the experimental data and result in a computational domain that is twice as wide as the nominal diameter of the largest parachute tested (WALRUS). To distinguish the parachute geometry from the freestream flow in the domain, the topoSet library is used. As mentioned by Greenshields [38], this assigns specific cells

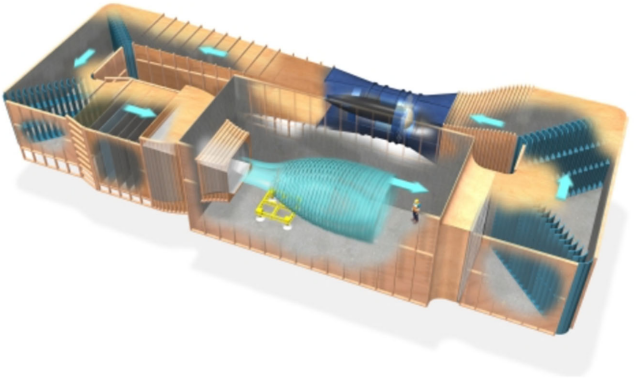

Fig. 9 Schematic of the Open-Jet Facility wind tunnel at Delft University of Technology [39].

in the computational domain as part of the parachute. These are then given properties corresponding to the material porosity of the parachute fabric. The selection of these properties and the resulting values are shown in Sec. III.D.2 and Table 3, respectively. Exact parameters of the blockMeshDict and topoSetDict files are included in Table 4.

The flow feature settings of the OpenFOAM simulations are selected to match the freestream conditions of the OJF before parachute deployment. Values for velocity and density are included in Table 5, and the associated boundary conditions are shown in Table 4 (they are the same for all three fields). It is important to note that the inletOutlet boundary condition corresponds to a zero-gradient boundary condition when the fluid flows out of the domain but fixes the boundary to a constant value when the flow is in the domain, as described by Greenshields [38]. The zero-gradient boundary conditions on the side walls are chosen to

Table 3 Material numerical properties of the DARE parachutes, obtained from destructive tensile tests

Property	Canopy	Suspension lines	Reinforcement tape
Material name	F111 Ripstop Nylon	Spectra	F111 Ripstop Nylon
K_0	0 N/m^2	0 N/m	0 N/m^2
K_1	30,006 N/m^2	211,895 N/m	3064.2 N/m^2
K_2	−18,936 N/m^2	489,633 N/m	68,823.4 N/m^2
γ	0.22	— —	0.05
a	65.98	— —	1206.7
b	37.45	— —	2858.33
ξ	0.2	0.2	0.2
ϵ	0.01	0.01	0.01
Δx, m	3.9e-4	3.9e-4	3.9e-4

Table 4 Summary of the OpenFOAM parameters used in the steady state flow simulations

Parameter Type	Parameter Name	Value
Simulation time features	t_0, s	0
	t_final, s	Set by residual error $<10^{-5}$
	Δt, s	1
Cartesian mesh features	Domain Size [x, y, z], m	[2,2,4]
	Resolution [x, y, z]	[100,100,150]
Boundary conditions	Inlet	Fixed value
	Side walls	Zero gradient
	Outlet	inletOutlet
Finite volume schemes	d/dt scheme	Default steady state
	Gradient schemes	Default Gauss linear
	Laplacian schemes	Gauss linear corrected
	Interpolation schemes	Default linear
	Divergence schemes	Bounded gauss upwind

Table 5 Steady-state experimental and simulated drag forces for the Stratos IV, WALRUS, and ringsail parachutes.

Parachute	Stratos IV					WALRUS					ADEPT ringsail		
Nominal velocity, m/s	10	15	20	25	30	10	15	20	25	30	10	20	30
Real velocity, m/s	8.85	16	20	25.4	27.1	9.1	15.1	21.1	25.2	27.4	9.6	18.9	27
Density, kg/m^3	1.202	1.196	1.199	1.204	1.2	1.203	1.211	1.21	1.2	1.204	1.21	1.203	1.205
Nominal surface area, m^2	1.715	1.715	1.715	1.715	1.715	3.37	3.37	3.37	3.37	3.37	0.792	0.792	0.792
Experimental drag force, N	43.1	100.2	187	281.4	400	73.5	172.1	297.2	415	621	27.5	105.6	223.4
Nonlinear drag force, N	43.3	97.44	173.2	275.03	396.1	73.9	166.31	295.7	415.9	598.9	26.25	100.3	213.8
Linear drag force, N	44.1	102.1	195.4	320.4	446.6	74.2	173.5	330.7	491.3	673.2	74.2	173.5	330.7
Cloth grid points	25,600	25,600	25,600	25,600	25,600	50,300	50,300	50,300	50,300	50,300	11,200	11,200	11,200
Cloth Sim. Time step, s	4e-7	4e-7	4e-7	4e-7	4e-7	4e-7	4e-7	4e-7	4e-7	4e-7	8.4e-7	8.4e-7	8.4e-7
Coupling iterations	7	6	9	11	12	8	8	7	9	11	14	15	12
Linear model error, %	**11.66**	**13.85**	**4.48**	**1.92**	**2.27**	**8.40**	**18.38**	**11.26**	**0.84**	**0.94**	**−8.44**	**5.54**	**2.07**
Non-linear model error, %	**−0.97**	**−2.26**	**−7.38**	**−2.75**	**0.46**	**−3.56**	**0.22**	**−0.50**	**−3.36**	**0.54**	**−4.30**	**−5.02**	**−4.55**

replicate the flow behavior just outside the test region of the OJF wind tunnel. The converged steady-state solution is reached when a residual of 10^{-5} is simultaneously yielded for the continuity, momentum, and energy equations.

For steady-state applications in compressible flow containing porous media, the standard recommended flow solver is rhoPorousSimpleFoam, which is based on solving the momentum equation across the finite computational domain. The converged steady-state solution is reached when a residual of 10^{-5} is simultaneously yielded for the continuity, momentum, and energy equations. Given that the steady-state pressure field is needed for the cloth deformation simulation, and not the transient behavior of the cloth fabric before inflation, the Reynolds-averaged Navier–Stokes equations are selected:

$$\overline{\frac{\partial}{\partial t}(\gamma\rho u_i)} + \overline{u_j \frac{\partial}{\partial x_j}(\rho u_i)} = -\frac{\overline{\partial p}}{\partial x_i} + \mu\overline{\frac{\partial \tau_{ij}}{\partial x_j}} + \overline{S_i} \quad \frac{\partial \overline{\rho}}{\partial t} + \overline{u_i}\frac{\partial \overline{\rho}}{\partial x_i} = 0 \tag{12}$$

Here, t denotes the time, x_i denotes the ith component of the spatial vector, u_i is the ith component of the velocity vector, ρ is the density of the fluid, p is the pressure within the fluid, and τ_{ij} is the viscous stress component which is directly influenced by the coefficient of proportionality μ. The momentum equation itself is modified to account for the presence of the porous medium itself. This is done first by adding a fabric porosity value γ to the time derivative of the equation and, second, by the addition of a source/sink term S_i. Using the Darcy–Forchheimer porosity model, S_i can be expanded according to

$$\overline{S_i} = -\left(\overline{\mu D_{ij}} + \frac{1}{2}\overline{\rho|u_{kk}|F_{ij}}\right)\overline{u_i} \tag{13}$$

where D_{ij} and F_{ij} are elements of the diagonal Darcy ($\boldsymbol{D}$) and Forchheimer ($\boldsymbol{F}$) matrices, as mentioned by Hafsteinsson [40]:

$$\boldsymbol{D} = \begin{pmatrix} D_{11} & 0 & 0 \\ 0 & D_{22} & 0 \\ 0 & 0 & D_{33} \end{pmatrix} \quad \boldsymbol{F} = \begin{pmatrix} F_{11} & 0 & 0 \\ 0 & F_{22} & 0 \\ 0 & 0 & F_{33} \end{pmatrix} \tag{14}$$

The values of these matrix terms are derived in Sec. III.D.2. The rhoPorousSimpleFoam solver solves the equations by using the Semi-Implicit Method for Pressure-Linked Equations (SIMPLE) algorithm. The k-omega turbulence model was adopted because of its high effectiveness in determining the pressure in the proximity to the surface of the parachute, which is crucial for the coupling with the cloth interaction. The model coefficients used for the k-omega model are the default ones by OpenFOAM and are shown in Table 6 [38].

2. *Porosity Modeling of the Canopy in Computational Domain*

Aquelet and Tutt [41] mention that the porosity of the fabric plays an important role in the drag performance, stability, and opening loads of the parachute itself. Therefore, the treatment of the parachute porosity in the OpenFOAM simulation is crucial to determining the elastic forces acting on the parachute geometry and the resulting deformation. The current OpenFOAM case setup accounts for this by using the adapted rhoPorousSimpleFoam flow solver, which uses the Darcy–Forchheimer porous media model. However, it is still unknown which values the Darcy and Forchheimer coefficients should take to reflect the canopy fabric. Aquelet and Tutt identify a close relationship between Darcy's law and the Ergun theory, which states that the forces acting on the surface of the porous media in contact with the fluid can be obtained through the integration of

Table 6 Summary of the coefficients used in the k-omega turbulence model for the OpenFOAM steady-state flow simulations

Parameter	Value	Parameter	Value
α_{k1}	0.85	γ_1	$\frac{5}{9}$
α_{k2}	1.0	γ_2	0.44
$\alpha_{\omega 1}$	0.5	β^*	0.09
$\alpha_{\omega 2}$	0.856	a_1	0.31
β_1	0.075	b_1	1.0
β_2	0.0828	c_1	10

$$\frac{dp}{d\hat{z}} = a(\mu,\gamma)\boldsymbol{v}_{\text{rel}}\boldsymbol{n}_s + b(\rho,\gamma)(\boldsymbol{v}_{\text{rel}}\boldsymbol{n}_s)^2 \tag{15}$$

over the entire discretized volume of the porous medium. In Eq. (15), $\boldsymbol{v}_{\text{rel}}$ refers to the relative velocity, $\hat{z}$ represents the local position along the fiber direction, $\boldsymbol{n}_s$ is the unit vector perpendicular to the shell, μ is the dynamic viscosity, and ρ is the density. The equation contains a linear and a quadratic term to describe the porous coupling forces on the fluid/porous structure interface. This matches the Darcy–Forchheimer equation, which also makes use of a linear and quadratic term to model the source/sink term in the momentum equation due to the porous media. Given that the Ergun theory is closely related to Darcy's law as described by Aquelet and Tutt, the coefficients a and b derived from Ergun theory are used as the Darcy–Forchheimer coefficients in the OpenFOAM case. For parachute applications, these can be derived using

$$a = \frac{150\mu(1-\gamma)^2}{D^2\gamma^3}t \qquad b = \frac{1.75\rho(1-\gamma)}{D\gamma^3}t \tag{16}$$

Note that t represents the thickness of the porous surface, and D is the characteristic length of the parachute, typically defined as $D = (6(1-\gamma)V/S)$ with V being the volume of the canopy and S its wetted surface area. While most of these parameters are geometric features of the parachute, which are to be analyzed, the porosity of the canopy fabric is a value that for certain cases may not be readily available. In such cases, the fabric porosity is derived by simulating a reference parachute of known material and measured drag

coefficient in the coupled OpenFOAM and cloth deformation simulation while varying the fabric porosity within a range of expected values. The resulting data in Fig. 10 show a linear correlation between the drag coefficient and the fabric porosity. The linear data are interpolated, leading to the expression

$$C_{D_{\text{SIV}}} = -1.7794\gamma + 0.9195R^2 = 0.9891 \tag{17}$$

where the Stratos IV drag coefficient is linked to the value of the porosity. The porosity can then be computed by matching the numerically obtained drag coefficient with the experimental value measured previously for the reference parachute. Such a calibration results in perfect estimations of drag force for that reference parachute geometry. This is shown in Fig. 11, in which the numerical and experimental drag force is plotted over time with different flow velocities. Once this porosity value is determined, it can be applied to other parachutes consisting of the same material, leading to high-accuracy drag results for those geometries as well (though not a perfect fit like in the case of the reference parachute). However, doing so may encode minor drag contributions specific to the Stratos IV parachute, such as those from the suspension lines, into the derived fabric porosity value. While these will match those of the WALRUS parachute, which is a scaled design of Stratos IV, it is believed they will induce small errors (less than 2%) in the ADEPT parachute simulations, based on the findings in

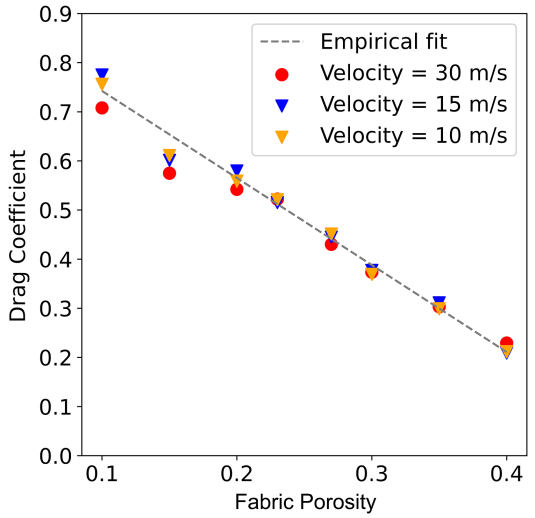

Fig. 10 Drag coefficient variation as a function of fabric porosity for varying flow velocities.

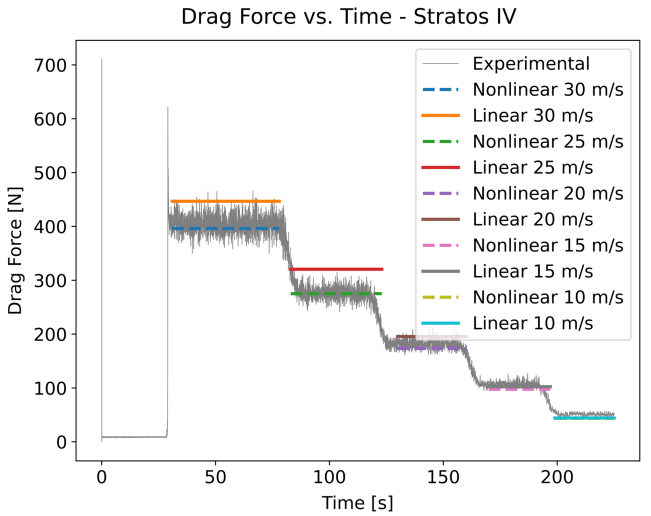

Fig. 11 The simulated and real steady-state drag force for the Stratos IV parachute at different wind-tunnel velocities.

[37]. Figure 10 shows the variation of the Stratos IV drag coefficient with fabric porosity, at different nominal flow speeds, from which Eq. (17) was obtained. One can see that changing the velocity does not have a large influence on the obtained linear expression. Furthermore, because this expression was obtained using the coupled OpenFOAM and cloth deformation simulation, the influence of a changing parachute geometry due to the change in flow speed is also taken into account and was found to not have a significant impact on the result. However, because the linear relation is obtained through numerical results for the drag coefficient, this analysis is limited to the range of applicability of Darcy's law and Ergun theory. A final aspect to note is the presence of random outliers in the plot, such as that for a fabric porosity value of 0.15. These most likely occurred due to a staircase effect resulting from the approximation of the parachute mesh as a porous medium in OpenFOAM's Cartesian mesh. To minimize this effect, many data points were used in the interpolation, and the flow mesh was recomputed for each of them with the parachute in a slightly changed position along the flow direction.

With the OpenFOAM case setup complete, the next step is to couple this porous medium CFD simulation with the Cloth Modelling Algorithm to generate the complete parachute inflation numerical model. This is the subject of the next section.

E. Coupling of Cloth Modeling Algorithm with OpenFOAM

The inflation procedure of a parachute is a complex FSI problem, requiring knowledge of both the shape of the parachute geometry and the surrounding flowfield at the same instance in time. This is best reflected in the required inputs of the cloth deformation algorithm and OpenFOAM simulation. The cloth deformation algorithm requires the elastic forces acting on the cloth, while the porous medium of the OpenFOAM simulation requires an accurate stereolithography geometry of the parachute. Therefore, the input of one numerical simulation clearly depends upon the output of the other, and separate independent analysis of these elements is not possible. To take this into account, a coupling procedure between the two algorithms is implemented to ensure simultaneous convergence of both the parachute canopy geometry and the surrounding flowfield, leading to the final inflated steady state of the parachute. The coupling procedure of the cloth modeling tool with the OpenFOAM simulation is described in Fig. 12.

At the beginning of the coupled simulation, the undeformed parachute geometry is initialized. For parachutes with circular cross-sections, this is defined as a flattened disk. The flowfield surrounding the parachute is also initialized with a constant pressure, velocity, and temperature field. Moreover, the boundary conditions of the fluid flow are also defined in the OpenFOAM simulation. With these settings put in place, the cloth deformation algorithm deforms the canopy with the initialized constant pressure field. Convergence is achieved, when the difference in the shape of the parachute geometry following successive iterations of stretching the mesh is less than a chosen threshold distance value. The difference in shape is determined by calculating the average difference in position of the mesh points which make up the parachute geometry. Mathematically, this is defined by

$$e = \frac{1}{n}\Sigma_{i=1}^{n}|\boldsymbol{X}_i^{k+1} - \boldsymbol{X}_i^{k}| \tag{18}$$

where n denotes the total number of mesh points, which make up the parachute geometry, and k is the number of the iterations, where the elastic forces were computed and the mesh was stretched before convergence. Lower threshold values of ϵ lead to a more refined deformed parachute shape, but at the expense of an increased number of iterations. The output of the cloth modeling algorithm is a STL file containing the converged shape of the parachute geometry. This is directly used as an input to the topoSet tool of the OpenFOAM simulation to define the porous medium. The OpenFOAM simulation computes the flow until the continuity equation is satisfied, which is indicative that the SIMPLE algorithm has converged, as described by Caretto et al. [42]. The output of the OpenFOAM simulation is a text file containing the updated pressure field of the fluid flow

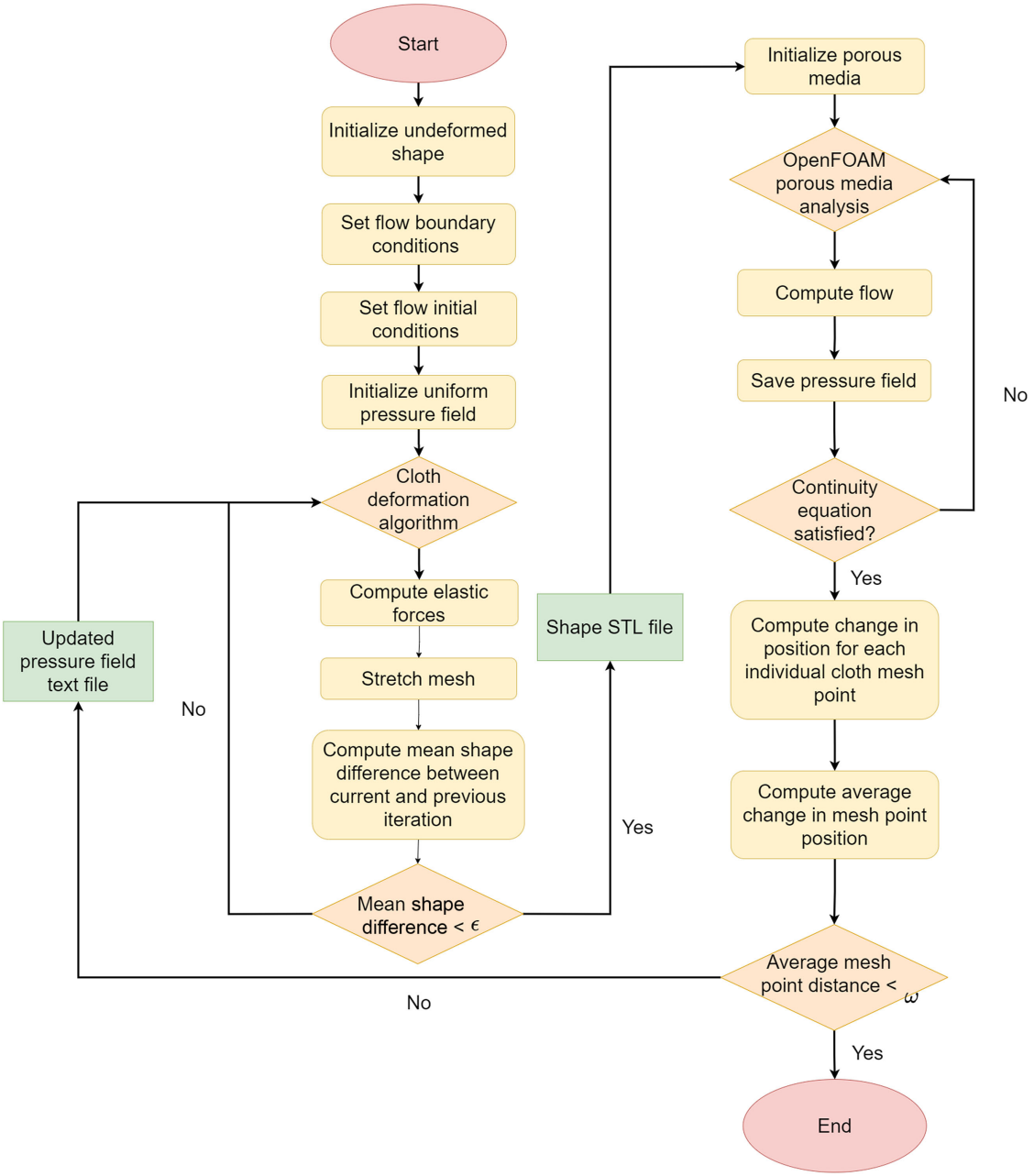

Fig. 12 Iterative coupling procedure for the steady state analysis of the fully inflated parachute.

surrounding the parachute. This updated pressure field can then be reentered into the cloth deformation algorithm to determine a better estimate of the deformed parachute geometry. This cycle makes up one iteration of the coupled simulation.

Following an iteration of the coupled simulation, to determine whether the shape has converged completely with the most updated pressure field, the same mathematical approach is taken as described by Eq. (18). However, this time around, the difference is computed between iterations of the coupled simulation, which includes the already converged stretched mesh and updated pressure field. This is not to be mistaken with checking the convergence of the cloth deformation algorithm only, where the iterations are simply pertaining to the stretching of the cloth mesh. Convergence is ensured by computing a nondimensional parameter error term ω, given as

$$\omega = \frac{\|X_{k+1} - X_k\|}{\|X_k\|} = \frac{R \cdot (\Delta x)^2}{S_0 \cdot K_{\text{Max}}} \tag{19}$$

where X_k is the position vector of the parachute cloth points at iteration k, R is the residual error from OpenFOAM, S_0 is the nominal area of the parachute, and K_{Max} is the maximum spring constant of the cloth. This can be directly linked to the residual error of the OpenFOAM simulation discussed earlier. Applying this strategy leads to the results discussed in Sec. IV.C.

F. Simulation Procedure for Transient Analysis

The procedure proposed in this paper for steady-state analysis can be repurposed to analyze the transient behavior of the cloth deformation algorithm for an inflating parachute geometry. This is done in a computationally robust manner by decoupling the cloth deformation model from the OpenFOAM simulation and therefore removing the need for coupled iterations between the two software programs. The transient analysis is therefore not a fluid/structure interaction model, and the need to calculate the added mass term to accurately link the flow simulations in OpenFOAM to the cloth deformation algorithm is also removed. However, to still account for the highly nonlinear and unsteady parachute inflation process [43], this paper proposes modeling the fluid behavior surrounding the parachute as the summation of two main aerodynamic forces. Such an approximation is sufficient for validating the transient behavior of the cloth model itself.

However, it is not expected for the simulations to perfectly match the experimentally obtained transient inflation behavior of the parachute. Differences in drag force values are possible due to inaccuracies in the flowfield approximation, but the frequency modes of the transient simulation should remain aligned, as this is purely a property of the cloth deformation algorithm. The air pressure acting on the internal surface of the canopy leading to the inflation of the geometry is the primary load acting on the parachute. However, in addition to this, a secondary global damping force acting on the external surface area of the canopy is added and resists this inflation. This is proposed here to account for the inertial effects of the air surrounding the parachute. When the parachute inflates, it applies pressure upon the surrounding air. By Newton's third law, this surrounding air must exert an equal and opposite force on the parachute, thereby resisting further inflation. The balance between these forces drives the transient behavior of the parachute shape from deployment until steady state. This is illustrated in Fig. 13 [44], in which F_P denotes the inflating force due to air pressure while F_D denotes the resistive damping force due to the inertia of the surrounding air.

To capture the transient behavior of the parachute inflation process, accurate estimates for both $\boldsymbol{F_P}$ and $\boldsymbol{F_D}$ are required. Estimates for $\boldsymbol{F_P}$ can be determined using the steady-state analysis procedure, which yielded a converged pressure field surrounding the inflated parachute. Using the pressure-field information, the pressure difference can be computed across all mesh points of the canopy. Averaging these individual pressure differences leads to an averaged inflation-distributed load due to air pressure. This constant value is applied as $\boldsymbol{F_P}$ across the complete canopy in the transient simulations.

To quantify the effect of damping due to the inertia of the surrounding air, $\boldsymbol{F_D}$ is modeled according to the damping equation

$$\boldsymbol{F_D} = -C_a \cdot \dot{\boldsymbol{X}}_{ij} \tag{20}$$

where C_a denotes the damping coefficient and $\dot{\boldsymbol{X}}_{ij}$ represents the absolute velocity of the mesh points of the parachute geometry itself. This added damping term, in effect, roughly models the effect added mass tensor on the parachute, while avoiding coupling with a fluid solver. It was found that a linear damping model was able to represent the inflation behavior to a sufficient level of accuracy, despite that spatial and time variations in pressure coefficient over the canopy surface were neglected, together with other inflation nonlinear phenomena. Therefore, more complicated damping models were not investigated for this application. The value of C_a depends on the porosity of the canopy material; however, analysis of the exact relationship between the two parameters is beyond the scope of this paper. Therefore, the value of C_a was determined by comparing the simulation results with the experimental wind-tunnel drag data for a reference parachute. Given that this coefficient is material dependent, once the value of C_a is determined through trial and error, this value can then be used for $\boldsymbol{F_D}$ for all other parachutes constructed using the same material.

Upon determining accurate estimates for $\boldsymbol{F_P}$ and $\boldsymbol{F_D}$, the transient simulation is conducted by applying these loads in the cloth deformation algorithm to stretch the canopy mesh nodes. Following every time step, when the canopy is stretched, the mesh-node positions are updated, and the elastic forces are computed once again due to $\boldsymbol{F_D}$ and $\boldsymbol{F_P}$. The computed elastic force in each suspension line is recorded, and the contribution in the direction of the axis of the parachute is computed. These contributions are then summed to determine the simulated drag force for each time step. These values are compared to load cell data recorded throughout the deployment sequence of the parachute in the wind tunnel, yielding the results shown in Sec. IV.E.

As a final consideration for the transient simulation, it is also important to consider the initial opening shape that is used. In the steady-state analysis, the main goal is to determine the final inflated shape of the parachute with only a few iterations. To reflect this, a flattened disk shape was chosen as the initial shape. However, in the case of the transient simulation, the inflation process of the parachute to its final state is of interest. Therefore, correct modeling of these phenomena depends on the initial canopy shape, which is reflective of the uninflated state of the parachute in real life. Realistic undeformed shapes for parachutes require cloth-to-cloth collision modeling. However, as this is very computationally expensive, an alternative initial folded shape is used and removes the need for such models. This folded shape is defined as follows: the disks of the parachute geometry are folded into cones, while the bands of the parachute are folded into cylindrical geometries. This is done using a zigzag folding pattern, which allows for the initial diameter to be reduced to an arbitrarily specified value. The lateral folding of the parachute thus assumes that the inflation process starts upon deployment. An illustration of this initial shape for a DGB parachute can be seen in Fig. 14.

IV. Results and Discussion

A. Validation Plan

The accuracy of the steady-state and transient formulations of the numerical model proposed in this study has been quantified using results from wind-tunnel tests of the parachutes outlined in Sec. II. This was done by comparing the drag forces recorded at different wind-tunnel nominal speeds with those simulated using this method. To recreate the parachutes digitally, the material properties deduced from the tensile tests presented in Sec. IV.B were used. Besides these, two important properties required by the model are the porosity of the canopy and reinforcement tape materials and the constant C_a. Given that these were impractical to measure with available equipment, a different approach was taken in determining them. Namely, out of the three case studies, the Stratos IV parachute wind-tunnel results were used to deduce the porosities and damping constants in question. This was done through a fine-tuning process of minimizing the error between the experimental drag force recorded for this parachute and the simulated one. As all parachutes are made from the same materials, the porosity and damping constant values deduced were then used in the simulations of the WALRUS and ADEPT ringsail parachutes. The correlation between the simulated and experimental

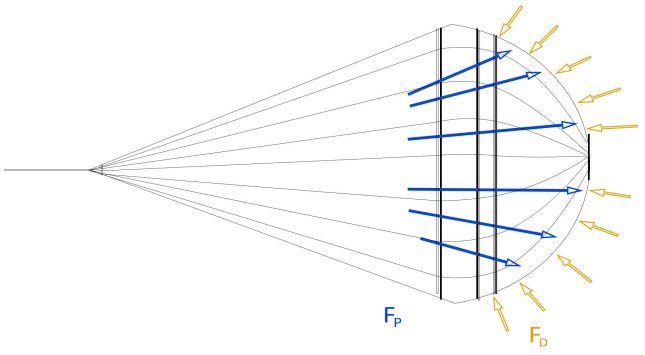

Fig. 13 Schematic showing the inflation and damping forces and their direction of action (inspired by [44]).

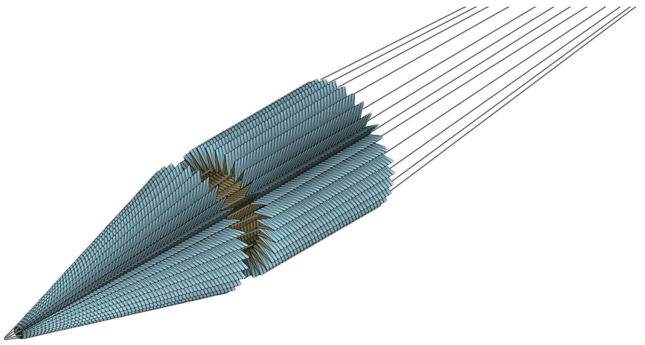

Fig. 14 Initial folded shape of the DGB parachute canopy in transient analysis.

drag forces of these latter two parachutes was only used for the validation of the model.

The plan for the validation includes two sets of simulations. The first set consists of eight steady-state simulations: five for the WALRUS parachute and three for the ADEPT parachute at nominal speeds between 10 and 30 m/s. These simulations produced one number each, representing the converged steady-state drag force, which was then compared with the average of the recorded load-cell force for a given wind-tunnel speed. The second set of simulations involved two transient simulations spanning the initial deployment shock of the WALRUS and ADEPT parachutes at a nominal speed of 30 m/s.

B. Material Tensile Test Results

The tensile tests performed on the canopy fabric, suspension lines, and reinforcement tape, outlined in Table 2 yielded the stress/strain curves shown in Figs. 15–18. It can be observed that the F111 Ripstop Nylon fabric displays a relatively linear behavior with deformation, for both the warp and weft directions. When loaded in shear, on the other hand, the fabric displays a nonlinear behavior for small strains, which asymptotes to a linear one as the fabric fibers are stretched. Overall, the resistance of the samples in 0/90 deg is significantly larger than at 45 deg due to the fiber alignment for these orientations. The suspension lines and reinforcement tape, on the other hand, display a highly quadratic resistance to strain, which asymptotes to a linear behavior as the failure strain is reached. These results link the discrepancy between a linear cloth model and the proposed nonlinear one to the seams of the parachute, and connection points with the suspension lines, and not to the canopy itself. Such a discrepancy would only accentuate with increasing flow velocity in real deployment conditions. Furthermore, these results are in line with those obtained in the studies performed by Amirkhizi et al. [45] and Bradford and Krieger [46]. In the former study [45], much like in this one, square samples of fabric were tested under uni-axial and bi-axial cyclic loadings in tension and shear. However, the much larger number of tests performed in this study reveals that the canopy behaves differently based on its loading history. More precisely, its resistance to strain decreases by a factor of 2 after its first loading cycle, and never fully recovers, implying that the tests performed in this study do not reveal the real cloth behavior experienced by a parachute in its most critical flight condition. The study performed by Bradford and Krieger, on the other hand, tensile tested under cyclic loads a large number of braided parachute suspension lines made from Spectra material. The authors of this study found, in a similar manner, a constantly changing elastic behavior with increasing number of load cycles for all samples. However, unlike the canopy samples, the present work found the repeated loading to induce a stiffening effect on the suspension lines. Nevertheless,

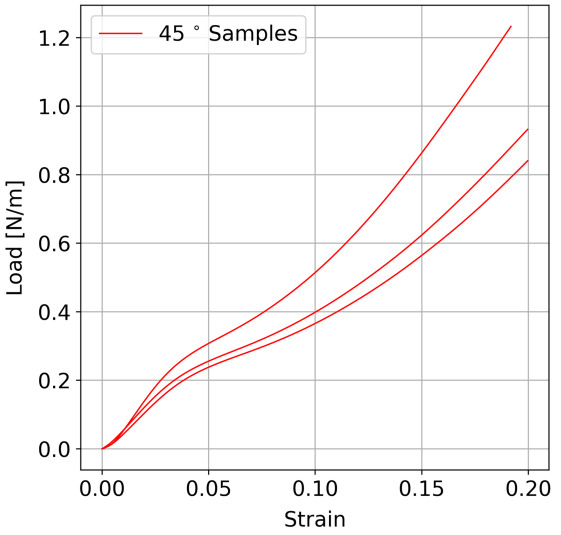

Fig. 16 Stress/strain plots for the 45 deg canopy tensile tests.

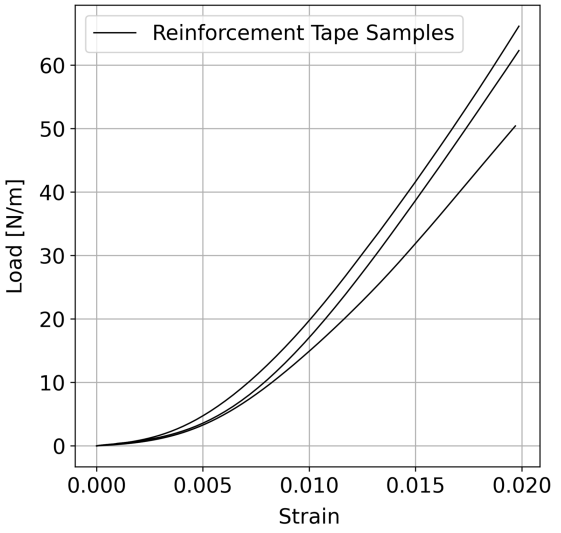

Fig. 17 Stress/strain plots for the reinforcement tape tensile tests.

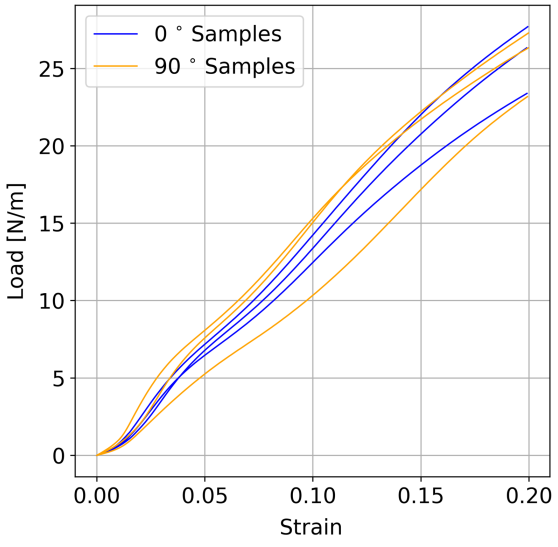

Fig. 15 Stress/strain plots for the 0 and 90 deg canopy tensile tests.

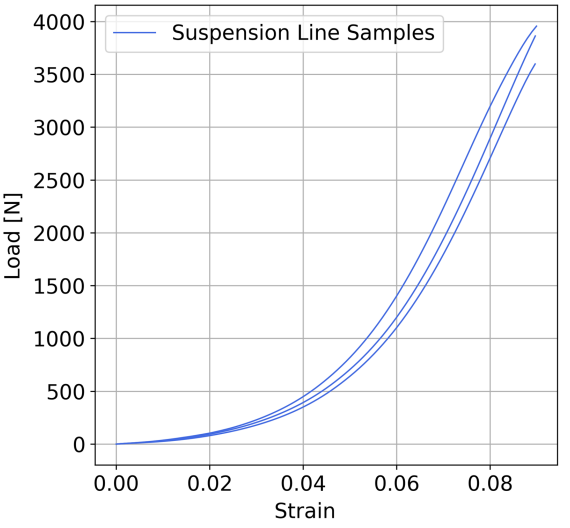

Fig. 18 Stress/strain plots for the suspension line tensile tests.

such wear-and-tear effects were minimized through the use of newly built prototypes for the wind-tunnel tests of the three parachute designs and were expected to be small due to the low-speed incompressible regime in which these were tested.

As described in Sec. III.A, the tensile tests performed have been recreated numerically, to obtain the numerical spring constants. Such an analysis provides a qualitative validation of the model, through the comparison of stretched numerical sample profiles with real ones. Figures 19 and 20 show the deformations of two canopy samples, oriented at 0 45 deg, respectively. In the left image of the figures, the deformation of the real canopy samples is shown, for a strain of 120%. The main difference between these deformations is their width variation along their length. The 0 deg sample shows a constant thickness everywhere. This is because only half of the fibers are loaded in this scenario, while the other half remains perpendicular to the load path. The simulated sample, shown on the right in Fig. 19, displays a mostly constant stress distribution, with relief zones close to the clamp centers. Based on the location of the maximum stress, this sample is expected to fail in the middle, which is what was observed in the real test. The 45 deg sample, on the other hand, shows thinning curvatures which lead to a minimum width at the center point between the two clamps. This is explained by the tendency of the fibers to orient themselves parallel to the load path, which leads to intrafiber shear deformations. The simulated deformation in Fig. 20 matches the real one, as confirmed by the stress distribution. Furthermore, four stress peaks can be observed at the corners of the simulated sample, which is consistent with the failure mode of the real one, in the bottom-left corner. Figure 21 provides two plots of the experimental and simulated elastic responses for the canopy samples described previously. A great fit can be observed between

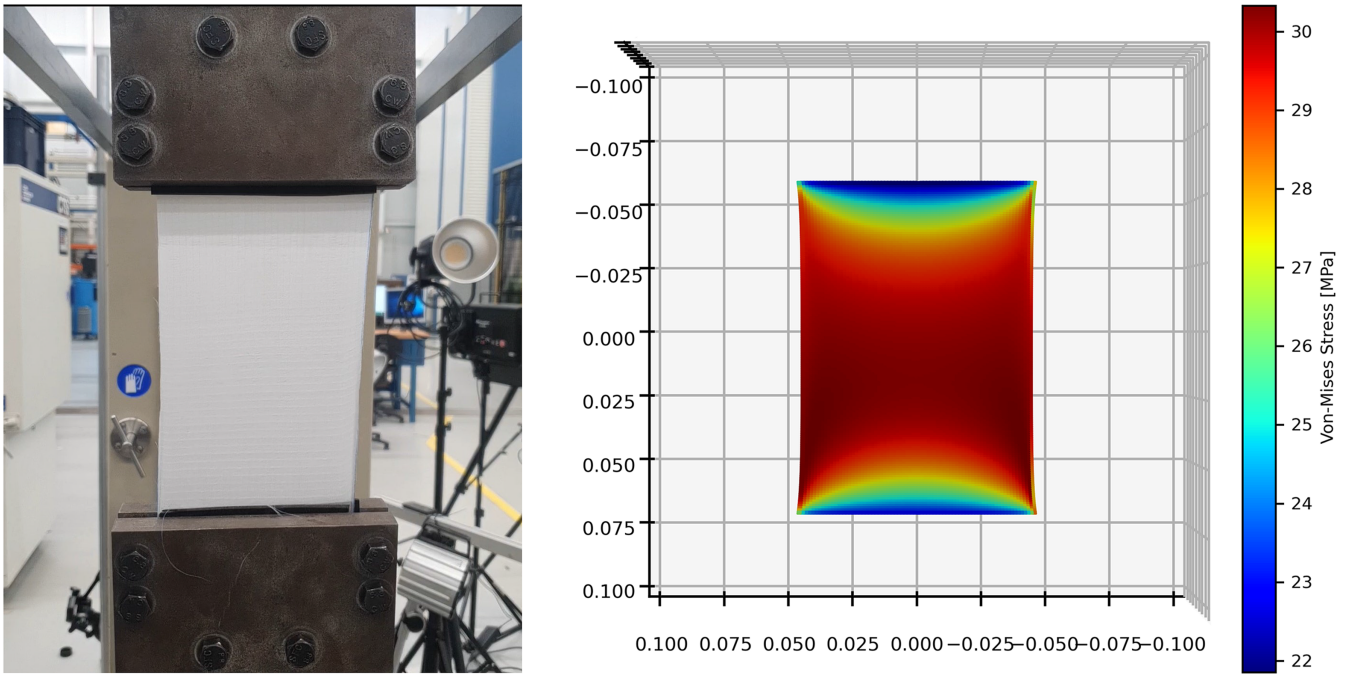

Fig. 19 Experimental vs simulated deformations of an F-111 Nylon woven fabric, at 0 deg, under a given tensile load. The simulated fabric has the von Mises stresses color mapped to it.

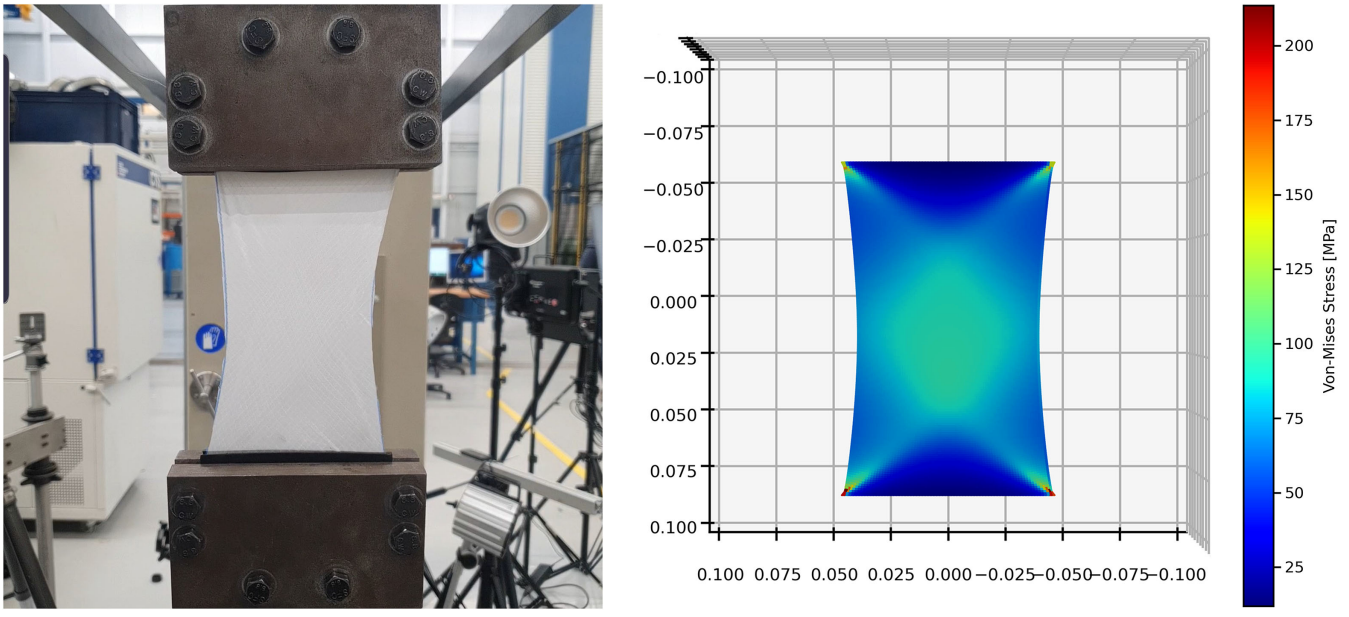

Fig. 20 Experimental vs simulated deformations of a F111 Nylon woven fabric, at 45 deg, under a given tensile load. The simulated fabric has the von Mises stresses color mapped to it.

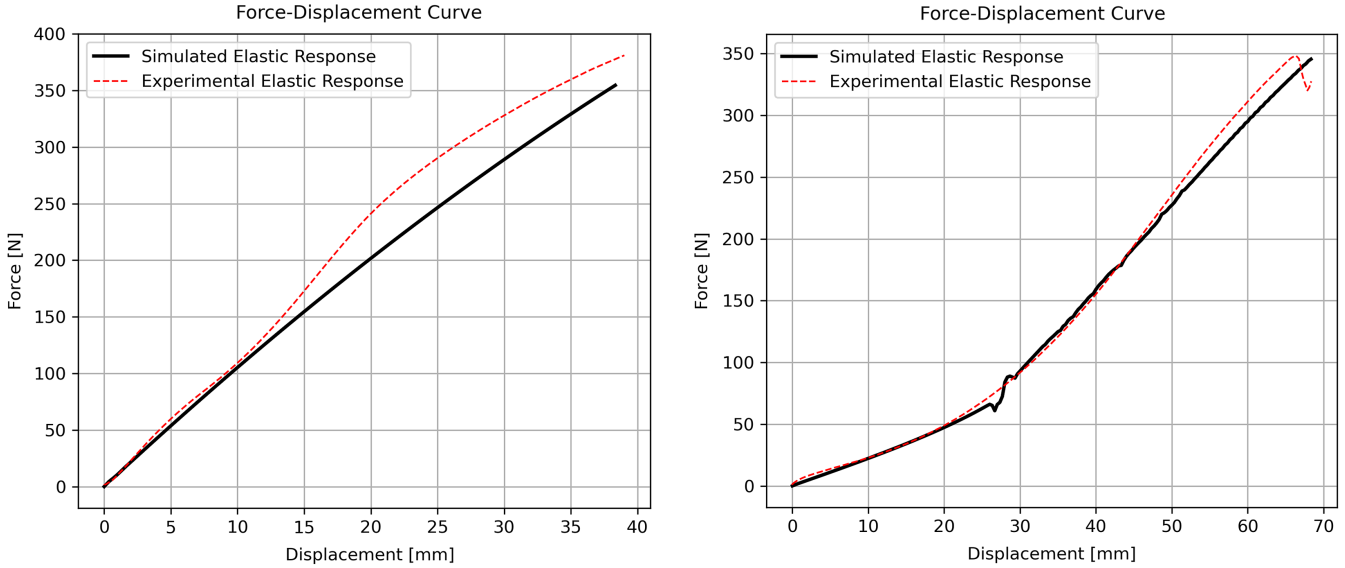

Fig. 21 The experimental (dotted red) and simulated (black) force-displacement curves of two canopy samples during tensile tests, at 0 (left) and 45 deg (right) orientations.

both curves, which is quantified by an R-squared value of $R^2 = 0.979$ for the 0 deg sample and $R^2 = 0.994$ for the 45 deg sample. This implies that second-degree polynomials are sufficient to describe the nonlinear behavior of parachute canopy materials and that a value of $\xi = 0.2$ is suitable to model the shear nonlinear springs. This result is further supported by the study performed by Bradford and Krieger [46], in which polynomials of the same order are found to accurately predict the strains of Spectra suspension lines.

The derived numerical cloth properties are summarized in Table 3. It should be noted that the linear cloth model used as a comparison in this study used only the K_1 constants for all the material types, whereas the nonlinear one used all of those displayed.

Three proportionality constants are presented in this table, K_0, K_1, and K_2, corresponding to the constant, linear, and quadratic contributions to the elastic response of the materials. For all of them, K_0 is 0 N, indicating that no residual stresses exist in the canopy, suspension lines, and reinforcement tapes when undeformed. The linear contribution K_1 is positive for all the materials, giving them their linear elastic properties under small deformations when the squared power of the displacement is negligible. For the quadratic elastic component, the canopy material shows a negative K_2, implying that its resistance to deformation decreases for large displacements, near its failure strain. On the other hand, a significant stiffening effect is observed for the suspension lines and reinforcement tape, which have a positive K_2. Porositywise, the canopy material is, by design, more porous than the reinforcement tape material, and therefore it exhibits smaller a and b coefficients. As the porosity of the suspension lines is not required by the proposed model, it was not calculated.

C. Steady-State Model Results

To validate the steady-state formulation of the simulation methodology proposed in this study, prototypes of each of the three parachute designs outlined in Sec. II have been developed and tested in the OJF wind tunnel. The testing procedure was as follows. Each parachute was placed in the middle of the wind tunnel's test section, to minimize wake effects. The wind tunnel was turned on, and the airspeed was varied in steps of 5 m/s starting from 30 down to 10 m/s. Both the nominal, preset speed and the real speed in front of the parachute were recorded. When a variation below 0.1 m/s was observed in the real speed, the measurement phase was initiated. The aerodynamic drag force acting on the parachute was measured with a load cell at a frequency of 100 Hz, until the end of the measurement phase, when the drag force for all nominal speeds had been measured for at least 20 s. One full-scale prototype has been developed for each of the aforementioned designs, using the same materials for the canopy, reinforcement tapes, suspension lines, and risers. The Darcy–Forchheimer coefficient matrices $\boldsymbol{D}$ and $\boldsymbol{F}$ of the canopy and reinforcement tapes needed by the porous media model presented in Secs. III.D.1 and III.D.2 were deduced with Eq. (15), based on the porosity value found for the Stratos IV parachute (see Sec. IV.A). Furthermore, the elastic behavior of these materials was determined through tensile testing of samples, as outlined in Sec. III.C. It was sufficient to quantify this behavior only through three polynomial constants, K_0, K_1, and K_2 for the canopy, suspension line, and reinforcement tape materials. The risers were assumed to be rigid in this analysis, and therefore no elastic response was determined for them. This was done because the wind-tunnel setup did not include real risers and instead attached the parachutes to the load cells through cords made from thick aramid fiber. These cords are significantly stiffer than the suspension lines, and therefore their deformation under the parachute drag forces was considered negligible. This simplification is expected to introduce an error in the transient model results only, which are outlined in Sec. IV.E.

The recorded and simulated steady-state drag forces for the WALRUS and ADEPT ringsail parachutes are shown in Fig. 22. The figure shows, plotted with dotted lines, the simulated forces for the series of wind-tunnel nominal velocities discussed in Sec. IV.A, against the recorded load-cell forces. For the WALRUS design, the 10, 15, 20, 25, and 30 m/s drag forces are plotted, while for the ringsail parachute, only the 10, 20, and 30 m/s are plotted. The results presented in the figure are summarized in Table 5, in which the difference between the linear and nonlinear simulated drag is quantified. The overprediction of the former for DGBs is attributed to the increased degree of fabric stretching when the quadratic behavior in Figs. 17 and 18 for the reinforcement tape and suspension lines, respectively, is approximated by a linear relationship, causing an excessive extension of the canopy shape. Conversely, in the case of ADEPT, the linear model results in an underprediction of drag because of the increased porosity as the canopy stretches. The errors between the simulated nonlinear and experimental drag forces are below 5% for both parachutes at all nominal velocities. This suggests a high correlation between the coupled numerical model and reality. The observed discrepancies can be attributed to a number of uncertainties in the testing procedure. These consist, first, of production errors in the parachute prototypes. As the canopy material is not isotropic, misalignments in the gore fiber directions between the simulated fabric and the real one could have led to uneven stretches in the fabric that would alter the drag of the parachute. Errors in the dimensions of the prototypes are also added to these. The most significant source of uncertainty, however, constitutes the porosity of the canopy material itself. As no tests were performed to determine this value, or the Darcy–Forchheimer coefficients themselves, only estimated values could be provided. A qualitative comparison between the simulated and recorded inflated shapes of the parachutes

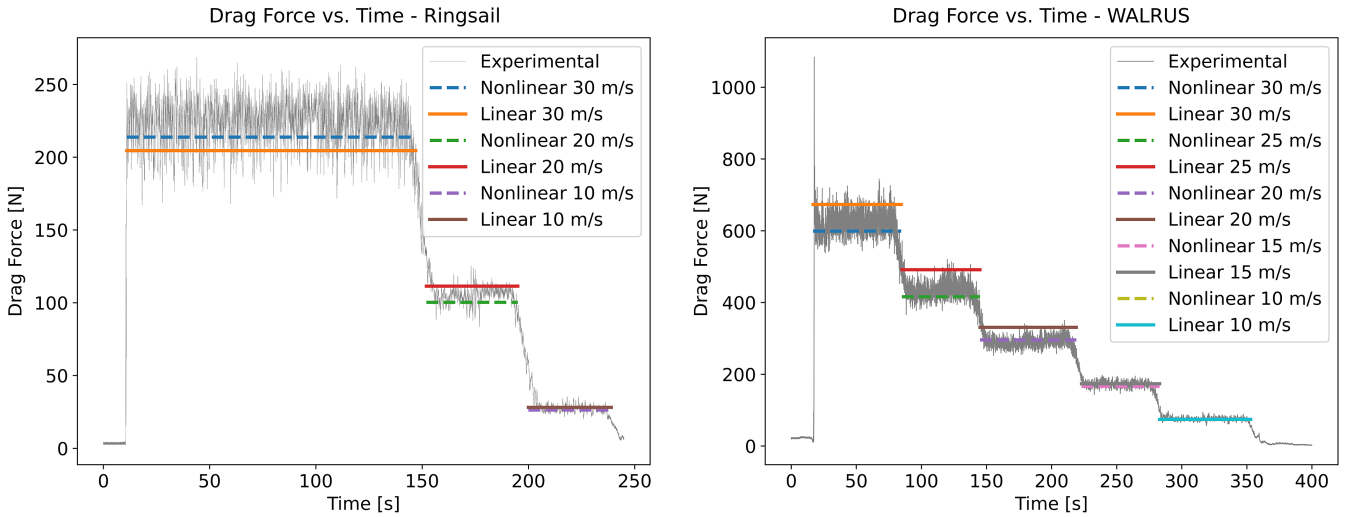

Fig. 22 Open-Jet Facility results: simulated and experimental steady-state drag forces for the WALRUS parachute (left); simulated and experimental steady-state drag forces for the ADEPT ringsail parachute (right).

was also performed. This is given in Figs. 23–25. All figures indicate a significant similarity between the inflated shapes of the real parachutes and the simulated meshes, which appears to validate the nonlinear cloth model outlined in Sec. III.A. Furthermore, the von Mises stresses shown on the simulated fabric seem to distribute in a radially symmetric pattern on the canopies. Stress concentrations can be observed as well at the connections between the suspension lines and the canopy for the Stratos IV and WALRUS parachutes, which was expected. Figures 26–28 additionally compare the drag coefficients of the three parachutes, produced with the linear and nonlinear models, to the recorded wind tunnel values for the considered nominal velocity range. Given the large correlation between aerodynamic forces, and the qualitative similarity in inflated parachute shapes, the steady-state implementation of the coupled numerical model presented in this paper appears to accurately portray reality for subsonic deployments.

D. Canopy Photogrammetric Analysis Results

The cross-sectional profile of the inflated parachute geometry obtained in the steady-state analysis is now compared with the actual inflated profile of the parachute obtained through wind-tunnel testing. This is done using a photogrammetric analysis of the images taken in the OJF facility of the inflated parachutes. During the wind-tunnel testing, numerous frames were taken of the inflated parachutes. These are averaged to remove instantaneous deviations in the parachute motions from the mean motion. The averaged images obtained from the OJF must first be corrected for the fish-eye distortion and perspective distortion generated by the camera and its positioning. Given the focal length of the lens used in the camera, the fish-eye lens distortion is readily corrected using the Lens Correction Filter in Adobe Photoshop 2022 [47]. However, as only one camera was used in the OJF for imaging, perspective distortion cannot be fully corrected for. Therefore, a geometric analysis is applied to relate the real geometrical features of the parachute to the features in the way they appear to the camera. This is done in two dimensions: lengths and diameters, as shown in Fig. 29. These dimensions are selected as diameters are easy to track in the images, especially near the corners. Furthermore, as the reinforcement tape has a large spring constant, the diameter of the band of the parachute will not deform much throughout the wind-tunnel testing. This serves as a useful reference point from which the other diameters and the perspective error can be characterized. The vertical length parameters allow for the lateral motion of the parachute to be evaluated. An illustration of the parachute and the perspective distortion of the camera can be visualized in Fig. 30. Given that the distance between the camera and the parachute (denoted as L, not to be mistaken with the L_{tot}, L_{disk}, and L_{band} parameters discussed in Fig. 29), and the apparent diameter of the parachute is known (depicted as D_{AP}), an expression for the difference between the real and apparent diameter is given as

$$\Delta D_P = L \tan\left(\arcsin\left(\frac{D_{AP}}{L}\right)\right) - D_{AP} \tag{21}$$

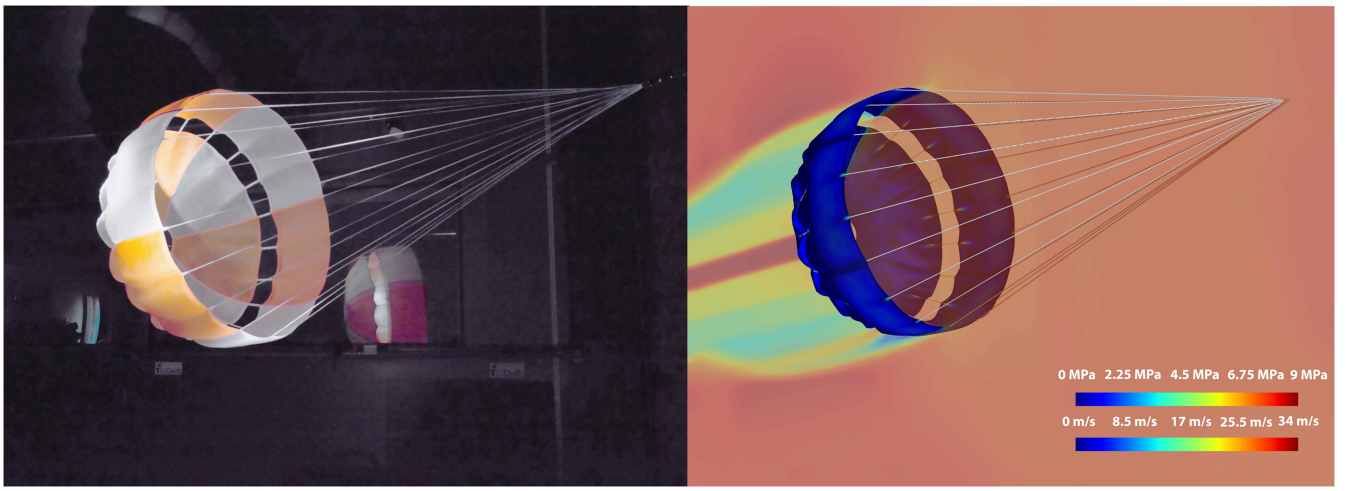

Fig. 23 Left: the inflated WALRUS parachute prototype in the OJF wind tunnel, at a nominal velocity of 30 m/s. Right: the simulated inflated WALRUS parachute, under the same conditions.

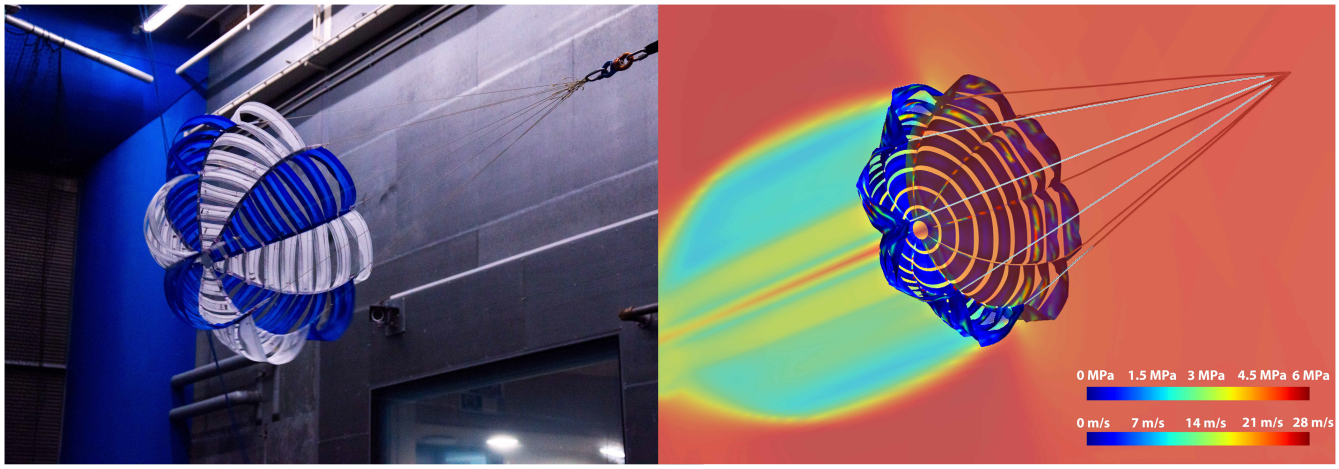

Fig. 24 Left: the inflated ADEPT ringsail parachute prototype in the Open-Jet Facility wind tunnel, at a nominal velocity of 30 m/s. Right: the simulated inflated ringsail parachute, under the same conditions.

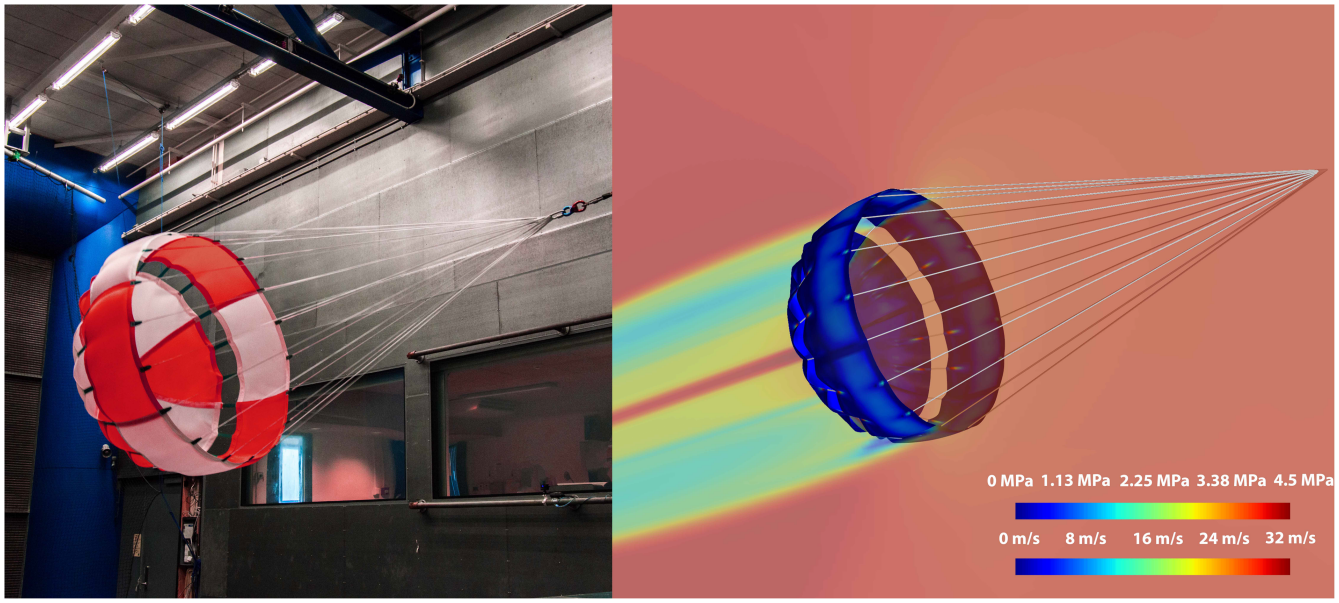

Fig. 25 Left: the inflated Stratos IV parachute prototype in the OJF wind tunnel, at a nominal velocity of 30 m/s. Right: the simulated inflated Stratos IV parachute, under the same conditions.

A similar approach can be taken with the lengths as well with the lengths of the parachute (this time with an apparent length L_{AP}). The equation for the length error is given as

$$\Delta L = \frac{2L}{2L - D_P} L_{AP} \tag{22}$$

The resulting parachute diameter and lengths, along with their corresponding errors and standard deviations, are included in Table 7. The comparison between the simulated and real parachute profile is visualized in Fig. 31, from which it is clear that the nonlinear model captures the real profile of the inflated parachute more accurately. This is attributed to the pronounced nonlinear stress/strain relationship measured for the suspension lines and reinforcement tape of the fabric, as described in Sec. IV.B. Although the canopy could be approximately described as a linear material for the considered loading conditions, the integration of nonlinear suspension lines and reinforcement tape dictates the need for a nonlinear cloth model.

E. Transient Model Results

The validation of the proposed model's transient implementation was performed through an analysis of the inflation behavior of the three parachutes considered: Stratos IV, WALRUS, and ADEPT. Each parachute was deployed three times in the wind tunnel at a nominal speed of 30 m/s. The force-time curves were, then, averaged together to obtain the experimental data used for validation. From these parachutes, only the latter two were used in the validation process. This process involves comparing the experimental and simulated drag variation through time for the duration of the inflation of the parachutes. As discussed in Sec. IV.A, the Stratos IV parachute transient drag-force data were used to determine the absolute damping coefficient of the material used for its canopy C_a by matching the simulated drag to the recorded one (see Sec. III.F). This was done through attempts to match two features of the deployment-force variation: the peak load and the inflation time. The inflation time was defined as the interval between the parachute deployment and the moment of the inflation, beyond which the force on the parachute is within 10% of the steady-state drag. The WALRUS and ADEPT parachutes' drag was subsequently simulated using this coefficient, given that both parachutes are made from the same materials. On top of the simulation parameters used in Table 3, the additional parameters used in the transient simulations are outlined in Table 8.

The deployment of either parachute was simulated assuming a constant pressure difference applied on the cloth Δp, computed by averaging the pressure difference variation on their canopies using

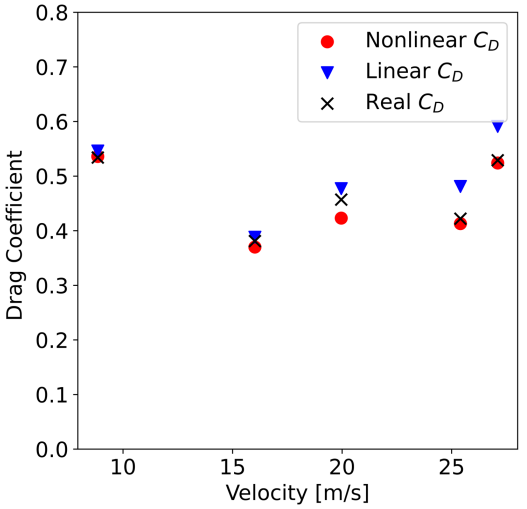

Fig. 26 Simulated and experimental coefficient variation with velocity for the Stratos IV parachute.

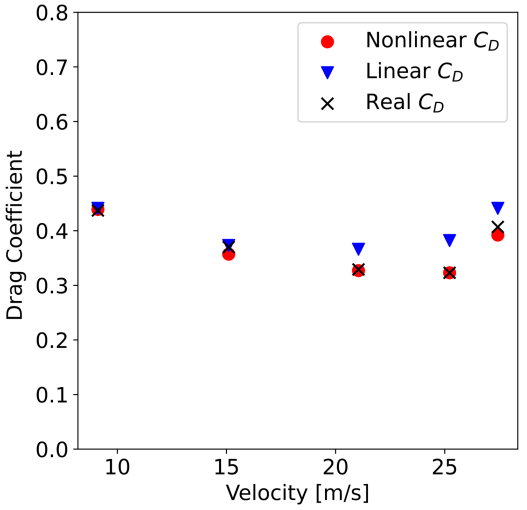

Fig. 27 Simulated and experimental coefficient variation with velocity for the WALRUS parachute.

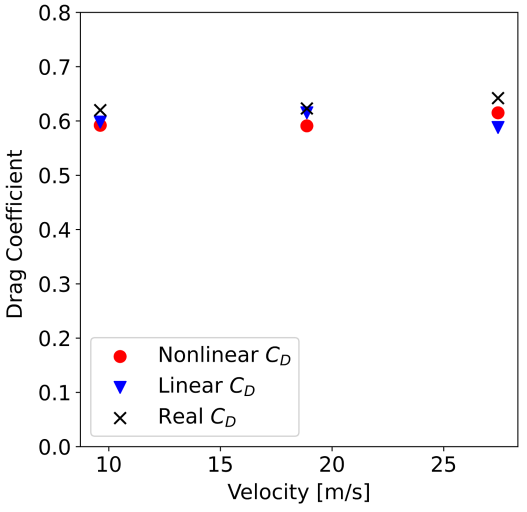

Fig. 28 Simulated and experimental coefficient variation with velocity for the ADEPT ringsail parachute.

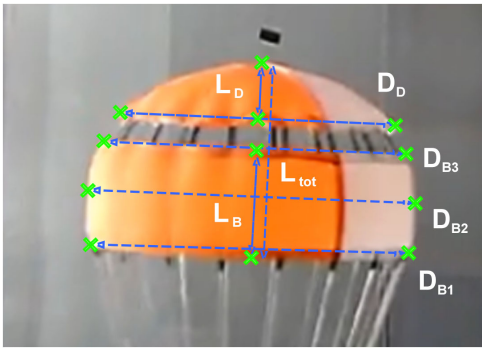

Fig. 29 Lengths and diameters used in photogrammetric analysis of OJF images.

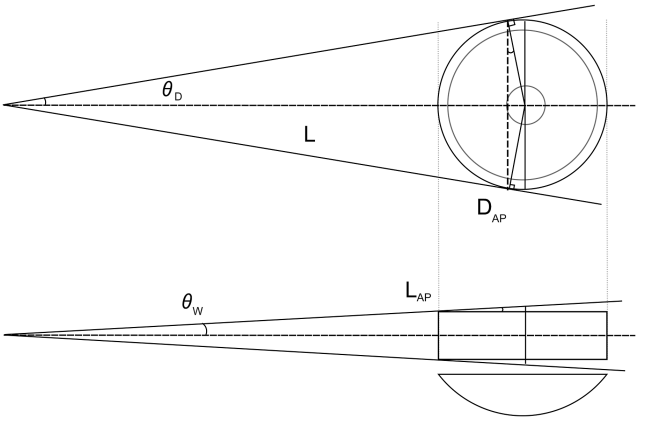

Fig. 30 Perspective correction method for the photogrammetric analysis of Stratos IV.

Table 7 Photogrammetric analysis results for the Stratos IV parachute

Parameter	Apparent mean value, m	Standard deviation, m	Corrected mean value, m
D_{st}	0.967	0	1
D_{mid}	0.9962	0.014	1.0327
D_{end}	0.9304	0.03	0.956
L_{tot}	0.603	0.012	0.516
L_{disk}	0.188	0.004	0.161
L_{band}	0.332	0.048	0.285

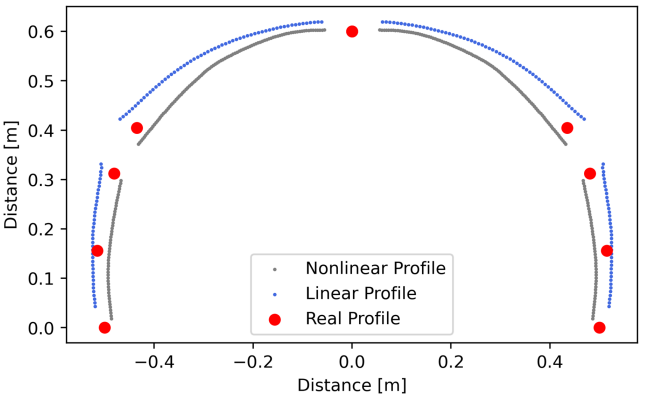

Fig. 31 Simulated linear and nonlinear profiles of the Stratos IV parachute for a nominal wind-tunnel velocity of 30 m/s, compared to the real parachute profile points.

Table 8 Initial parameters for the transient simulations of the Stratos IV, WALRUS, and ADEPT parachutes

Parameter	Stratos IV	WALRUS	ADEPT
Density, kg/m^3	1.202	1.204	1.205
Velocity, m/s	27.1	27.43	27
Δp, Pa	184	221	355
C_a, Ns/m	8.2	8.2	8.2
Initial radius, m	0.1	0.2	0.1

the steady-state implementation of the proposed model. This should yield the same drag force as the simulations performed in Sec. IV.C in steady state. Both parachutes were simulated under a nominal wind-tunnel speed of 30 m/s, and their shapes as well as drag forces were recorded as a function of time. On a qualitative level, the simulated inflation behavior seems to match the experimental one for the last two instances in time. In the first instance, the experimental shape of the parachute appears more chaotic than the simulated one. This discrepancy is most likely attributed to the initial conditions of the simulation. While in the wind-tunnel experiments, the WALRUS parachute was deployed from a parachute bag that introduced lateral oscillations in the parachute, the numerical mesh was folded symmetrically, as described in Sec. III.F. This was done, as the interactions between the parachute bag and the canopy were impractical to simulate, and would have compromised the robustness of the model. Figure 32 plots the experimental and simulated drag force variation for the reference Stratos IV parachute, while Figs. 33 and 34 plot these quantities for the WALRUS and ADEPT parachutes.

Several observations can be made about the mentioned plots. To begin with, a close match can be observed between the experimental and simulated peak loads for all three parachutes. The simulated peak value for Stratos IV is 698 N, whereas the experimental value is 621 N, leading to an error of 12.4%. Similarly, the simulated peak value for the WALRUS parachute is 1227 N, while the experimental value is 1102 N, leading to an error of 11.3%. Finally, ADEPT shows an experimental peak of 251 N, against a simulated one of 262 N, leading to a 4.4% error. All simulations seem to overestimate the inflation by a similar, small amount, which implies that the damping coefficient C_a introduced in Sec. III.F is indeed a material property. Furthermore, this systematic error can be explained by the assumption of a constant pressure difference applied to the canopy throughout the entire inflation. While this assumption seems to hold in the steady state, as can be seen in the flattened parts of these plots, it is an overestimation of the initial part of the inflation, when the parachute is closed. The additional elastic energy built up in this initial stage of the deployment could be a significant contribution to these errors. To further reduce these errors, the damping force can be

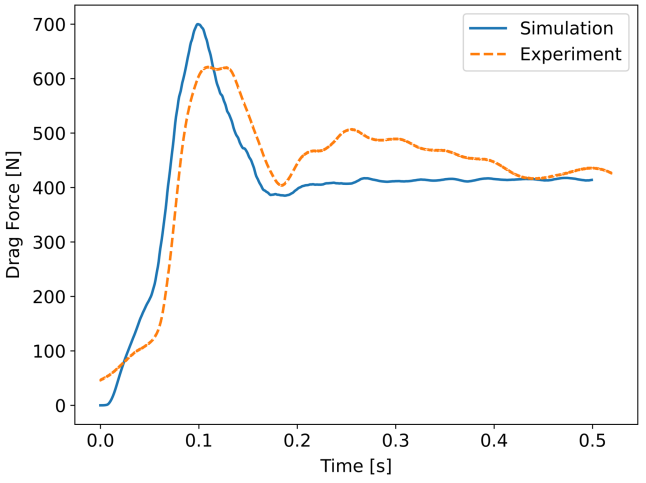

Fig. 32 The experimental and simulated drag forces for the Stratos IV parachute prototype at a nominal wind-tunnel speed of 30 m/s.

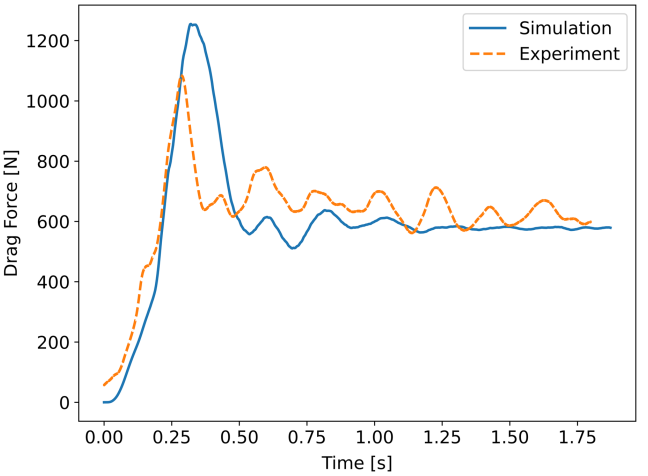

Fig. 33 The experimental and simulated drag forces for the WALRUS parachute prototype at a nominal wind-tunnel speed of 30 m/s.

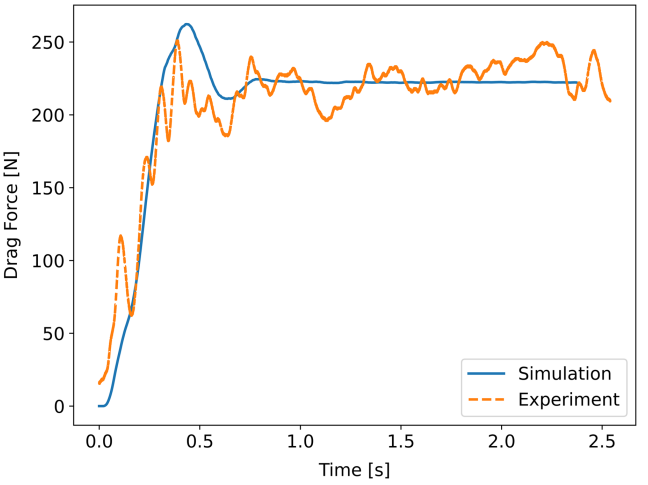

Fig. 34 The experimental and simulated drag forces for the ADEPT ringsail parachute prototype at a nominal wind-tunnel speed of 30 m/s.

rewritten to include a quadratic dependence on velocity as well, through one more damping constant, which might increase the precision of the transient implementation of the model. However, introducing multiple damping constants into the model would make the present method impractical and diminish its robust nature. Another discrepancy between the experimental and simulated drag curves constitutes the random high-frequency noise observed for all parachutes, but especially for ADEPT. Given that Kalman filtering was used on the measured signals, the observed discrepancy could be explained by the lateral oscillations of the parachutes in the wind tunnel, due to disturbances in the incoming flow and the effect of the parachute bag release. These are phenomena that require transient CFD coupling to be simulated and would compromise the robustness of the model. In addition to the potential effects of experimental disturbances, the oscillatory phase difference is also attributed to the overdamping predicted by the numerical C_a due to the simplified profile of the assumed pressure distribution. Moreover, the cloth-to-cloth collision was considered beyond the scope of this work. Nevertheless, the high-frequency modes and associated drag peaks are adequately predicted for the considered case studies, implying that the sole determination of the spring-to-mass ratio is sufficient to capture the correct elastic behavior of the cloth. In Fig. 35, three different instances in time are portrayed for the real WALRUS parachute canopy, as well as the simulated one, using the parameters and procedure outlined previously

Given the high correlation between the experimental transient drag behavior and the simulated one, at both the quantitative and

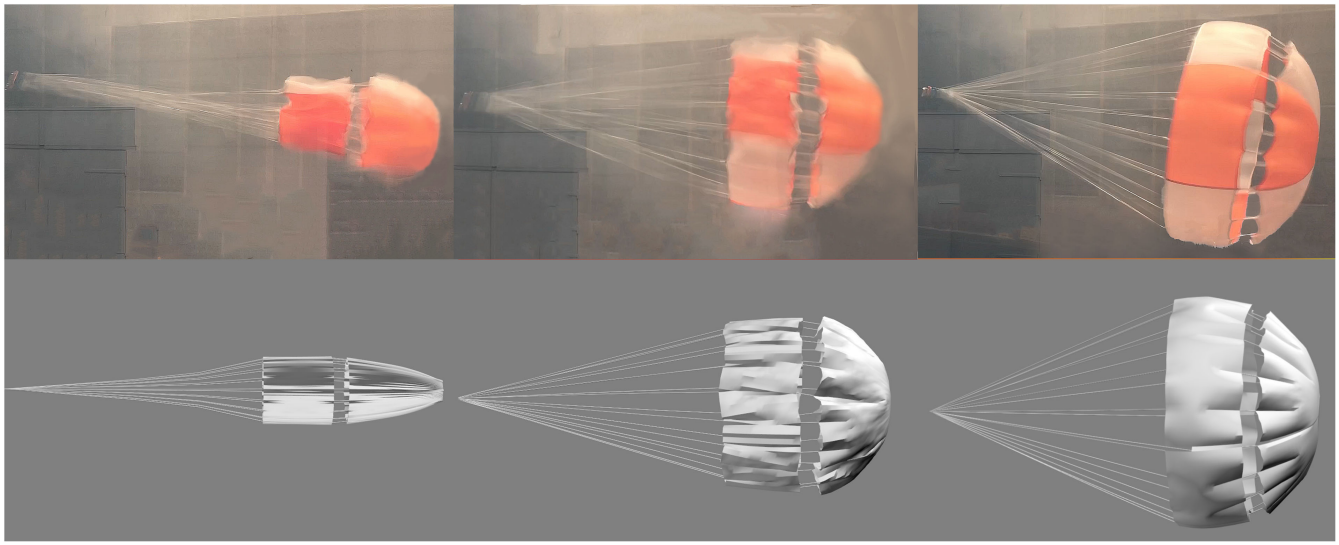

Fig. 35 Comparison between the real and simulated parachute canopy shapes of the WALRUS design at different instances in time throughout their inflation at 30 m/s of nominal wind-tunnel velocity.

qualitative levels, it can be concluded that the transient implementation of the coupled model proposed in this paper is validated.

V. Conclusions

The novelty of this paper lies in the development of a nonlinear mass-spring model used to evaluate the structural dynamic of parachutes based on empirical data for the axial, shear, and bending spring stiffness of the parachute's fabric, seams, and suspension lines. The implementation of polynomial expressions in Provot's differential equation for modeling the deformation of parachute cloth material results in a robust numerical cloth model in which no matrix formulation is required, because the nonlinear elastic response of the deformable structures is evaluated locally, with every node of the cloth mesh depending only on its neighboring nodes. The implication of such a model, verified by means of tensile testing of canopy material, is that the nonlinearity of parachute fabric can be modeled by means of polynomial equations of an arbitrary degree. Moreover, the shear and bending stresses within the textile fabric can be modeled with a lumped-mass system by using proportionality constants with respect to the axial stress. The parachute cloth is thus capable of developing wrinkling in response to the bending caused by the velocity field. When stretching fabric material at an angle of 45 deg, in fact, a large component of the load is taken by fibers parallel to the loading direction, while a smaller fraction is perceived in the form of friction and compression between the twines.

The results discussed in this work revealed that the iterative algorithm proposed for the steady-state implementation of the numerical model coupling the cloth deformation and the computational flow dynamics resulted in a unique parachute shape and flowfield condition after six iterations for each set of initial conditions assigned. While the deformation of the canopy could be approximately described by a linear relationship for the range of low speeds tested, the nonlinearity of the suspension lines and reinforcement tapes is rather pronounced even at low velocities. Accounting for this effect has been found to better characterize the drag coefficient of DGBs. Larger uncertainty has been measured for the ringsail parachute, where the more complex arrangements of the sails increase its geometric porosity. This is supported by the direct correlation identified between porosity, which was modeled by combining the Darcy–Forchheimer equation with Ergun's theory, and the experimental drag force measured in the OJF. Such a correlation was validated by the close agreement between the simulated and the experimental aerodynamics for all the case studies, which yielded steady-state errors below 5% for all considered conditions.

To model the transient behavior of the parachute inflation, the summation of two aerodynamic forces was considered, namely, the air pressure acting on the internal canopy surface and the damping force acting on the external area to account for inertial forces. This approach was validated by comparison of the simulated peak load and the experimental equivalent, which yielded errors between 4.4 and 12.4% for the three case studies considered. It was found that the method proposed overestimated the initial pressure, likely due to the presence of elastic energy buildup, which can be modeled with an additional damping force dependent on velocity. More accurate results could be achieved with polynominal expressions describing the damping behavior. However, alternative methods would need to be proposed to compute the associated damping constants other than recursive approaches, which could prove impractical.

Finally, this work unveiled the dependency of the simulated transient behavior with the initial folding configuration of the parachute. The comparison of the aerodynamic data measured in the OJF for the three case studies showed that the presence of a folding bag created additional lateral oscillations associated with an increased level of noise in the drag measurements. Nevertheless, given the difficulty in modeling such an inherent aerodynamic instability, this paper proposed the use of a symmetric folding configuration for increased robustness in the simulations.

Acknowledgments

The authors would like to thank the members of the Parachute Research Group from the Delft Aerospace Rocket Engineering student society, for providing the experimental wind-tunnel data of the Stratos IV, WALRUS, and ADEPT ringsail parachutes. They would also like to acknowledge the staff at the Faculty of Aerospace Engineering at Delft University of Technology for providing access to the OJF wind tunnel and the Delft Aerospace Structures and Materials Laboratory.

References

[1] Peterson, C., Strickland, J., and Higuchi, H., "The Fluid Dynamics of Parachute Inflation," *Annual Review of Fluid Mechanics*, Vol. 28, No. 1, 1996, pp. 361–387. https://doi.org/10.1146/annurev.fl.28.010196.002045

[2] Jodehl, J., Anton, S., Bosboom, T., Dhiyaneeswaran, S., Dvorak, O., Homola, M., Knöll, N., Menting, E., Sujahudeen, M., and Pepermans, L., "Architectures for Parachute Testing," *72nd International Astronautical Congress*, International Astronautical Federation Paper IAC-21, D2,3,4,x64184, 2021.

[3] Farhat, C., Rallu, A., Wang, K., and Belytschko, T., "Robust and Provably Second-Order Explicit-Explicit and Implicit-Explicit Staggered Time-Integrators for Highly Non-Linear Compressible Fluid-Structure Interaction Problems," *International Journal for Numerical*

Methods in Engineering, Vol. 84, No. 1, 2010, pp. 73–107. https://doi.org/10.1002/nme.2883

[4] Potvin, J., Bergeron, K., Brown, G., Charles, R., Desabrais, K., Johari, H., Kumar, V., McQuilling, M., Morris, A., Noetscher, G., and Tutt, B., "The Road Ahead: A White Paper on the Development, Testing and Use of Advanced Numerical Modeling for Aerodynamic Decelerator Systems Design and Analysis," *21st AIAA Aerodynamic Decelerator Systems Technology Conference and Seminar*, AIAA Paper 2011-2501, 2011. https://doi.org/10.2514/6.2011-2501

[5] Lingard, J., and Darley, M., "Simulation of Parachute Fluid Structure Interaction in Supersonic Flow," *18th AIAA Aerodynamic Decelerator Systems Technology Conference and Seminar*, AIAA Paper 2005-1607, 2005. https://doi.org/10.2514/6.2005-1607

[6] Lingard, J., Darley, M., Underwood, J., and Brown, G., "Simulation of the Mars Science Laboratory Parachute Performance and Dynamics," *19th AIAA Aerodynamic Decelerator Systems Technology Conference and Seminar*, AIAA Paper 2007-2507, 2007. https://doi.org/10.2514/6.2007-2507

[7] Tutt, B., Richard, C., Roland, S., and Noetscher, G., "Development of Parachute Simulation Techniques in LS-DYNA," *11th International LS-DYNA Users Conference*, Livermore Software Technology Corp., Detroit, 2010, pp. 25–36, https://www.dynalook.com/conferences/international-conf-2010/Simulation-5-3.pdf [retrieved 15 May 2022].

[8] Lingard, J. S., Underwood, J. C., Darley, M. G., Marraffa, L., and Ferracina, L., "Supersonic Tests of the Double Gap Disk-Gap Band Parachute and Fluid Structure Interaction Simulation," *23rd AIAA Aerodynamic Decelerator Systems Technology Conference*, AIAA Paper 2015-2109, 2015. https://doi.org/10.2514/6.2015-2109

[9] Le Garrec, M., Poncet, A., and Lapoujade, V., "Parachute Deployment Simulation Using LS-DYNA\ICFD Solver and Strong FSI Coupling," *12th European LS-DYNA Conference*, DYNAmore GmbH, Stuttgart, Germany, 2019, pp. 1–15, https://www.dynalook.com/conferences/12th-european-ls-dyna-conference-2019/fluid-structure-interaction/le-garrec_dynas.pdf [retrieved 15 May 2022].

[10] Hill, J. L., and Braun, R., "Implementation of a Mesomechanical Material Model for IAD Fabrics Within LS-Dyna," *AIAA Aerodynamic Decelerator Systems (ADS) Conference*, AIAA Paper 2013-1367, 2013. https://doi.org/10.2514/6.2013-1367

[11] Taylor, T., "An Investigation of the Apparent Mass of Parachutes Under Post Inflation Dynamic Loading Through the Use of Fluid Structure Interaction Simulations," *17th AIAA Aerodynamic Decelerator Systems Technology Conference and Seminar*, AIAA Paper 2003-2104, 2003. https://doi.org/10.2514/6.2003-2104

[12] Yu, H., Pantano, C., and Cirak, F., "Large-Eddy Simulation of Flow over Deformable Parachutes Using Immersed Boundary and Adaptive Mesh," *AIAA Scitech 2019 Forum*, AIAA Paper 2011-2501, 2019. https://doi.org/10.2514/6.2019-0635

[13] Huang, D. Z., De Santis, D., and Farhat, C., "A Family of Position- and Orientation-Independent Embedded Boundary Methods for Viscous Flow and Fluid–Structure Interaction Problems," *Journal of Computational Physics*, Vol. 365, July 2018, p. 74–104. https://doi.org/10.1016/j.jcp.2018.03.028

[14] Huang, Z., Avery, P., Farhat, C., Rabinovitch, J., Derkevorkian, A., and Peterson, L. D., "Simulation of Parachute Inflation Dynamics Using an Eulerian Computational Framework for Fluid-Structure Interfaces Evolving in High-Speed Turbulent Flows," *2018 AIAA Aerospace Sciences Meeting*, AIAA Paper 2018-1540, 2018. https://doi.org/10.2514/6.2018-1540

[15] Borker, R., Huang, D., Grimberg, S., Farhat, C., Avery, P., and Rabinovitch, J., "Mesh Adaptation Framework for Embedded Boundary Methods for Computational Fluid Dynamics and Fluid-Structure Interaction," *International Journal for Numerical Methods in Fluids*, Vol. 90, No. 8, 2019, pp. 389–424. https://doi.org/10.1002/fld.4728

[16] Kim, Y., and Peskin, C. S., "2–D Parachute Simulation by the Immersed Boundary Method," *SIAM Journal on Scientific Computing*, Vol. 28, No. 6, 2006, pp. 2294–2312. https://doi.org/10.1137/s1064827501389060

[17] Kim, Y., and Peskin, C. S., "3-D Parachute Simulation by the Immersed Boundary Method," *Computers & Fluids*, Vol. 38, No. 6, 2009, pp. 1080–1090. https://doi.org/10.1016/j.compfluid.2008.11.002

[18] Purvis, J. W., "Prediction of Parachute Line Sail During Lines-First Deployment," *Journal of Aircraft*, Vol. 20, No. 11, 1983, pp. 940–945. https://doi.org/10.2514/3.56727

[19] Purvis, J., "Numerical Prediction of Deployment, Initial Fill, and Inflation of Parachute Canopies," *8th Aerodynamic Decelerator and Balloon Technology Conference*, AIAA Paper 1984-0787, 1984. https://doi.org/10.2514/6.1984-787

[20] Strickland, J., Porter, V., Homicz, G., and Gossler, A., "Fluid-Structure Coupling for Lightweight Flexible Bodies," *17th AIAA Aerodynamic Decelerator Systems Technology Conference and Seminar*, AIAA Paper 2003-2157, 2003. https://doi.org/10.2514/6.2003-2157

[21] Li, X., "Verification and Validation of the Spring Model Parachute Air Delivery System in Subsonic Flow," Final Progress Rept., Univ. at Stony Brook, Albany, NY, 2015. https://doi.org/10.21236/ada623612

[22] Pepermans, L., Menting, E., Rozemeijer, M., Britting, T., and Derks, P., "Trajectory Simulations and Sensitivity for the SPEAR Parachute Test Vehicle," International Astronautical Congress, Washington, D.C., 2019, https://www.researchgate.net/publication/336721870_Trajectory_Simulations_and_Sensitivity_for_the_SPEAR_Parachute_Test_Vehicle [retrieved 15 May 2022].

[23] Menting, E., Pepermans, L., and Soliman, B. K. E., "Evolution and Evaluation of the DARE Large Envelope Advanced Parachute System," Flight Vehicles, Aerothermodynamics and Re-Entry Missions Engineering (FAR), Capitolo, Italy, 2019, https://www.researchgate.net/publication/336140513_Evolution_and_Evaluation_of_the_DARE_Large_Envelope_Advanced_Parachute_System [retrieved 15 May 2022].

[24] Menting, E., Pepermans, L., Britting, T., Soliman, E., Klaassen, J., Rozemeijer, M., and van't Hof, J., "Flight Testing of Parachute Recovery Systems Aboard REXUS," *Proceedings of the 3rd Symposium on Space Educational Activities, Leicester*, Univ. of Leicester, Leicester, U.K., 2020, pp. 176–180. https://doi.org/10.29311/2020.44

[25] Géczi, M., Kandiyoor, L. P. G., and Dvorak, O., "Development of a Low Cost, Low Altitude Test Vehicle for High Dynamic Pressure Parachute Testing," *IAC Conference Proceedings*, International Astronautical Federation Paper IAC-20,D2,6,8,x56366, 2020, https://www.researchgate.net/publication/344366051_Development_of_a_low_cost_low_altitude_test_vehicle_for_high_dynamic_pressure_parachute_testing [retrieved 15 May 2022].

[26] Britting, T., Joosten, I., Koops, B., Toussaint, W. L. J. R., Sujahudeen, M. S., Vukosavljević, K., Knöll, N. E., Casablanca, A., Dighe, N., Scholts, S. O., and Kumar, S., "Design, Manufacture, and Validation of a Student-Made Ringsail Parachute for Sounding Rocket Recovery," *4th Symposium on Space Educational Activities*, Polytechnic Univ. of Catalonia, Barcelona, Spain, 2022, pp. 749–755. https://doi.org/10.5821/conference-9788419184405.129

[27] Britting, T., Toussaint, W. L. J. R., Vukosavljević, K., Sujahudeen, M. S., Knöll, N. E., Pepermans, L., and Hadji, Y. P., "Selection Criteria for Parachutes of Student-Built Sounding Rockets," *4th Symposium on Space Educational Activities*, Polytechnic Univ. of Catalonia, Barcelona, Spain, 2022. https://doi.org/10.5821/conference-9788419184405.133

[28] Pepermans, L., Oliver Scholts, S., Menting, E., Britting, T., Lopez Rivera, A., Dhiyaneeswaran, S., Toussaint, W., Bosboom, T., and Koops, B., "Integration of the Large Envelope Advanced Parachute System in Stratos IV," *71st International Astronautical Congress*, International Astronautical Federation Paper IAC-20,D2,3,8,x58488, 2020.

[29] Giaquinta, D., "The Flow Topology of the Ahmed Body in Cross-Wind: An Experimental Investigation by means of Robotic Volumetric PIV," M.Sc. Thesis, Delft Univ. of Technology, Delft, The Netherlands, 2018, https://repository.tudelft.nl/islandora/object/uuid:27b75b3f-8b4d-4977-82ee-e531fd986839?collection=education [retrieved 15 May 2022].

[30] Knacke, T. W., "Parachute Recovery Systems Design Manual," Naval Weapons Center TR 9207158, China Lake, CA, 1991, http://ftp.demec.ufpr.br/CFD/bibliografia/aerodinamica/PARACHUTE\%20Recovery\%20Systems\%20Desgin\%20Manual.pdf [retrieved 15 May 2022].

[31] Weil, J., "The Synthesis of Cloth Objects," *Association for Computing Machinery,* Vol. 20, No. 4, 1986, pp. 18–22.

[32] Blinn, J. F., "Simulation of Wrinkled Surfaces," *Seminal Graphics*, Vol. 1, July 1998, p. 111–117; Reprinted with Permission from Computer Graphics, Vol. 12, No. 3, July 1978, 286–292. https://doi.org/10.1145/280811.280982

[33] Provot, X., "Deformation Constraints in a Mass-Spring Model to Describe Rigid Cloth Behaviour," *Graphics Interface*, Canadian Information Processing Soc., Mississauga, Canada, 1995, pp. 147–155.

[34] Baraff, D., and Witkin, A., "Large Steps in Cloth Simulation," *Proceedings of the 25th Annual Conference on Computer Graphics and Interactive Techniques*, Assoc. for Computing Machinery, New York, 1998,

p. 43–54.
https://doi.org/10.1145/280814.280821
[35] Hairer, E., Lubich, C., and Wanner, G., "Geometric Numerical Integration Illustrated by the Störmer–Verlet Method," *Acta Numerica*, Vol. 12, May 2003, pp. 399–450.
https://doi.org/10.1017/S0962492902000144
[36] OpenCFD, Ltd., OpenFOAM, Software Package, Ver. 9 2004, https://www.openfoam.com/ [retrieved 15 May 2022].
[37] Bergeron, K., Ecklebe, D., McClure, K., Johari, H., Curlett, T., and Pitman, B., "Parachute Suspension Line Drag Analysis," *20th AIAA Aerodynamic Decelerator Systems Technology Conference and Seminar*, AIAA Paper 2009-2982, 2009, pp. 1–17.
https://doi.org/10.2514/6.2009-2982
[38] Greenshields, C., *OpenFOAM v9 User Guide*, OpenFOAM Foundation, London, England, U.K., 2021, https://doc.cfd.direct/openfoam/user-guide [retrieved 15 May 2022].
[39] "Open Jet Facility," Delft University of Technology, Delft, The Netherlands, 2020, https://www.tudelft.nl/lr/organisatie/afdelingen/flow-physics-and-technology/facilities/low-speed-wind-tunnels/open-jet-facility [retrieved 15 May 2022].
[40] Hafsteinsson, H. E., "Porous Media in OpenFOAM," Chalmers Univ. of Technology, Gothenburg, Sweden, 2009.
[41] Aquelet, N., and Tutt, B., "Euler-Lagrange Coupling for Porous Parachute Canopy Analysis," *International Journal of Multiphysics*, Vol. 1, No. 1, 2007, pp. 53–68.
https://doi.org/10.1260/175095407780130517
[42] Caretto, L. S., Gosman, A. D., Patankar, S. V., and Spalding, D. B., "Two Calculation Procedures for Steady, Three-Dimensional Flows with Recirculation," *Proceedings of the Third International Conference on Numerical Methods in Fluid Mechanics*, edited byH. Cabannes, and R. Temam, Springer-Verlag, Berlin, Heidelberg, 1973, pp. 60–68.
[43] Yu, L., Cheng, H., Zhan, Y., and Li, S., "Study of Parachute Inflation Process Using Fluid–Structure Interaction Method," *Chinese Journal of Aeronautics*, Vol. 27, No. 2, 2014, pp. 272–279.
https://doi.org/10.1016/j.cja.2014.02.021
[44] Sengupta, A., Wernet, M., Roeder, J., Kelsch, R., Witkowski, A., and Jones, T., "Supersonic Testing of 0.8 m Disk Gap Band Parachutes in the Wake of a 70 deg Sphere Cone Entry Vehicle," *20th AIAA Aerodynamic Decelerator Systems Technology Conference and Seminar*, AIAA Paper 2009-2974, 2009, pp. 1–17.
https://doi.org/10.2514/6.2009-2974
[45] Amirkhizi, A. V., Blanas, M., Campos, F., Krantz, K., Drane, P., and Sherwood, J., "Material Characteristics of F-111 (PIA-C-44378) Canopy Fabric in Uniaxial and Biaxial Conditions," *26th AIAA Aerodynamic Decelerator Systems Technology Conference*, AIAA Paper 2022-2724, 2022.
[46] Bradford, G. O., and Krieger, H., "Investigation of Tensile and Torsional Properties of Braided Parachute Suspension Line," *24th AIAA Aerodynamic Decelerator Systems Technology Conference*, AIAA Paper 2017-4198, 2017, pp. 1–11.
https://doi.org/10.2514/6.2017-4198
[47] "Correct Image Distortion and Noise," Adobe, Inc., San Jose, CA, 2023, https://helpx.adobe.com/photoshop/using/correcting-image-distortion-noise.html [retrieved 15 May 2022].

R. M. Cummings
Associate Editor